Dynamics of excited electronic states in functional materials

RAQUEL ESTEBAN-PUYUELO

UPPSALA
UNIVERSITET

Abstract

Esteban-Puyuelo, R. 2021. Dynamics of excited electronic states in functional materials. *Digital Comprehensive Summaries of Uppsala Dissertations from the Faculty of Science and Technology* 2028. 77 pp. Uppsala: Acta Universitatis Upsaliensis. ISBN 978-91-513-1179-1.

Non-equilibrium processes involving excited electron states are very common in nature. This work summarizes some of the theoretical developments available to study them in finite and extended systems. The focus lays in the class of Mixed Quantum-Classical methods that describe electrons as quantum-mechanical particles but approximate ionic motion to behave classically. In particular, Non-Adiabatic Molecular Dynamics and Real Time Density Functional Theory are described and applied to answer questions regarding non-equilibrium dynamics in diverse functional materials. First, the effect of phase boundaries and defects in monolayer MoS_2 samples is studied. This material has been suggested as a good candidate to substitute silicon in many applications, such as flexible electronics and solar cells. It is known that defects and different polymorphs are present in experimental samples, and therefore it is extremely important to understand how realistic samples perform. We present how the electron-hole recombination times are accelerated in presence of defects, as well as how the structural changes in samples that mix several phases of MoS_2 affect their electronic structure. After that, rectangular graphene nanoflakes are explored. As an application to finite systems, we show in rectangular graphene nanoflakes how different magnetic configurations have distinct optical absorption spectra and how this can be used for opto-electronic applications. Furthermore, the high harmonic generation for different magnetic couplings is studied, showing how some harmonics can be suppressed or enhanced depending on the underlying electronic structure. Finally, diffuse scattering in SnSe is investigated in an experimental collaboration in order to understand how phonon-phonon interactions affect the scattering dynamics, which may lead to profound insight into its thermoelectric properties.

Raquel Esteban-Puyuelo, Department of Physics and Astronomy, Materials Theory, Box 516, Uppsala University, SE-751 20 Uppsala, Sweden.

A mi familia, aquí y allí

List of papers

This thesis is based on the following papers, which are referred to in the text by their Roman numerals.

I **Role of defects in ultrafast charge recombination in monolayer MoS$_2$**
Raquel Esteban-Puyuelo and Biplab Sanyal
arXiv:2103.13386 (2021), in revision in *Phys. Rev. B*

II **Complexity of mixed allotropes of MoS$_2$ unraveled by first-principles theory**
Raquel Esteban-Puyuelo, D.D. Sarma, and Biplab Sanyal
Phys. Rev. B **102**, 165412 (2020)

III **Tailoring the opto-electronic response of graphene nanoflakes by size and shape optimization**
Raquel Esteban-Puyuelo, Rajat Kumar Sonkar, Bhalchandra Pujari, Oscar Grånäs, and Biplab Sanyal
Phys. Chem. Chem. Phys., **22**, 8212-8218 (2020)

IV **Graphene nanoflakes as a testbed for electronic structure analysis through high harmonic generation**
Raquel Esteban-Puyuelo, Biplab Sanyal, and Oscar Grånäs
Manuscript

V **Visualizing nonequlibrium atomic motion and energy transfer in SnSe**
Amit Kumar Prasad, Raquel Esteban-Puyuelo, Pablo Maldonado, Shaozheng Ji, Biplab Sanyal, Oscar Grånäs, and Jonas Weissenrieder
Manuscript

Reprints were made with permission from the publishers.

Comments on my contribution

Papers I-V are the result of close collaborations with the coauthors.

Paper I

I participated in the design of the project, performed all the calculations and analysis and participated in discussions. I mainly wrote the manuscript and handled its submission.

Paper II

I performed all the calculations and analysis. I participated in the discussions, mainly wrote the paper and managed the replies to the referees.

Paper III

I participated in the design of the study and performed all the calculations (except the NWChem benchmark done by RKS). I participated in the discussions with the collaborators, mainly wrote the paper and managed the replies to the referees.

Paper IV

Participated in the design of the project and performed the HHG calculations. I contributed to the analysis of the results, and wrote the manuscript together with OG.

Paper V

I performed the phonon and phonon-phonon simulations and participated in the discussion, analysis and interpretations of the results. I contributed to the writing of the manuscript.

Publications not included in this thesis

■ **Enhanced Gilbert damping in Re-doped FeCo films: Combined experimental and theoretical study**
Serkan Akansel, Ankit Kumar, Vijayaharan A. Venugopal,
Raquel Esteban-Puyuelo, Rudra Banerjee, Carmine Autieri, Rimantas
Brucas, Nilamani Behera, Mauricio A. Sortica, Daniel Primetzhofer,
Swaraj Basu, Mark A. Gubbins, Biplab Sanyal, and Peter Svedlindh
Phys. Rev. B **99**, 174408 (2019)

■ **Structural phase transition in monolayer gold(I) telluride: From a room-temperature topological insulator to an auxetic semiconductor**
Xin Chen, Raquel Esteban-Puyuelo, Linyang Li, and Biplab Sanyal
Phys. Rev. B **103**, 075429 (2021)

Contents

1. Introduction

Sólo el que sabe es libre, y más libre el que más sabe.
(Only the one who knows is free, and freer the one who knows more)

Miguel de Unamuno

We have been using tools even since before we became humans. Choosing natural materials and modifying them to suit our needs is a part of the development of our species, and tools have been evolving accordingly from stone knives to plastic bottles and mobile phones. We are surrounded by electronics: from the simplest digital watch to the Perseverance Rover from NASA that is exploring Mars, our world depends on efficient electronic devices. For more than a century, they have been successfully made from bulk semiconductors such as silicon, and they have become smaller with time. However, miniaturization and improvement in efficiency have reached a plateau, since quantum confinement and thermal losses play an important role when three-dimensional structures reach a small enough size. One of the routes towards smaller scales is to build devices made from two-dimensional materials, since their surface area to volume ratio is maximal. Graphene, a single layer of graphite, has been theoretically studied extensively since the 1950s [1] but not until its first experimental realization in 2004 [2], it became a promising alternative to silicon-based electronics. Despite its extremely interesting properties (extraordinarily high electron mobility and flexibility, to name a few), graphene is a semimetal, and the corresponding lack of energy band gap limits its usage in semiconductor devices. One option to overcome this issue is to functionalize graphene in order to open up a gap, for example by introducing defects [3] that modify its electronic structure, or by creating nanoribbons and nanoflakes [4]. These nanostructures are highly sensitive to size and shape due to quantum confinement, and multiple efforts have been made to predict and characterize their properties, for instance looking at their optical signatures. Another trend has been the investigation of other 2D materials beyond graphene, either 2D allotropes such as borophene, silicene, germanene, stanene, or compounds like hexagonal boron nitride and transition metal dichalcogenides (TMDs) [5, 6]. TMDs are bulk materials composed of single layers bound together via weak van der Waals forces, which can be exfoliated. MoS_2, one of the most studied TMDs and an indirect band gap semiconductor of 1.29 eV in its bulk form,

shifts to having a 1.8 eV direct gap in its most stable 2D phase. A direct gap is more efficient, which is why it is a promising candidate to substitute silicon in miniaturized electronic devices. Two-dimensional and bulk layered materials have been investigated with other applications in mind, and one of which is the exploitation of their capability to convert thermal into electrical energy. Thermoelectric materials such as SnSe [7, 8] lead a way into environmentally friendly power generation processes, and therefore studying their fundamental properties at the atomic scale is crucial for the development of this field.

Many of the applications in which all these materials can be used are out of equilibrium. In fact, most of nature's phenomena occur far from the ground state and are the response of a system after a perturbation. However, they have been historically tackled with methods that are within the Born-Oppenheimer approximation (decoupling of electron and ionic degrees of freedom), which is strictly valid only in the ground state and some particular transient situations. The question of how to correctly study phenomena that involve excited electronic states has been around for a long time, and the quantum chemistry and experimental fields have done very important advances. Time-resolved experiments such as transient absorption spectroscopy are extensively used to study the relevant timescales and mechanisms [9], as well as excitonic properties [10]. Very accurate theoretical solutions exist for small systems such as atoms and small molecules [11], but extended systems such as 2D materials and bulk solids still pose a challenge. Many approximations need to be made, and the most important one is the neglect of the quantum nature of the ions composing the material. These groups of methods, in which ions are treated classically and electrons quantum-mechanically, are called semiclassical methods and they are the basis of what will be discussed in this thesis.

2. Theory and methods

The aim of this chapter is to provide a background on the theory and methods that serve as a basis for the projects that conform this thesis. I start in section 2.1 with the full quantum mechanical description of the time-dependent many-body problem, and then introduce the Mixed Quantum-Classical Dynamics by approximating the ionic motion as classical. I continue in section 2.2 by treating the electronic system in the effective framework given by Time-Dependent Density Functional Theory, and finish the approximations path by considering time-independent or ground state Density Functional Theory. Furthermore, in section 2.3 I discuss lattice vibrations through the concept of phonons, in order to introduce the rate equations that describe the transfer of energy between the electronic and phononic system.

Atomic units are used in this text unless otherwise stated ($e^2 = \hbar = m_e = 1$), so distances are measured in Bohr and energies in Hartree.

2.1 Excited state dynamics

2.1.1 The full quantum problem

To exactly calculate time-dependent properties of an isolated non-relativistic many-body system, one needs to solve the time-dependent Schrödinger equation (TDSE), which can be written as follows:

$$i\frac{\partial \Psi(\mathbf{R},\mathbf{r},t)}{\partial t} = \mathscr{H}_F \Psi(\mathbf{R},\mathbf{r},t). \qquad (2.1)$$

$\Psi(\mathbf{R},\mathbf{r},t)$ is a short hand notation for the total wavefunction $\Psi(\mathbf{r}_1, \mathbf{r}_2, ...\mathbf{r}_N, \mathbf{R}_1, \mathbf{R}_2, ..., t)$, which depends on the positions of the electrons $\{\mathbf{r}_i\}$ and the ions $\{\mathbf{R}_I\}$, as well as the time t. The full Hamiltonian operator is defined as

$$\mathscr{H}_F = T_e + T_{nuc} + V_{e-n} + V_{e-e} + V_{n-n} + V_{ext}. \qquad (2.2)$$

The first two terms in (2.2) are the kinetic energies of the electrons and ions, the third term stands for the Coulomb interaction between electrons and ions,

the fourth and fifth terms represent the electron-electron and ion-ion interaction and the last one is an external potential. More explicitly,

$$\mathscr{H}_F = -\frac{1}{2}\sum_i \nabla_i^2 - \sum_I \frac{1}{2m_I}\nabla_I^2 - \sum_{i,I} \frac{Z_I}{|\mathbf{r}_i - \mathbf{R}_I|} +$$
$$\frac{1}{2}\sum_{i\neq j} \frac{1}{|\mathbf{r}_i - \mathbf{r}_j|} + \frac{1}{2}\sum_{I\neq J} \frac{Z_I Z_J}{|\mathbf{R}_I - \mathbf{R}_J|} + V_{ext}, \qquad (2.3)$$

where m_I is the mass of the Ith ion and Z_I is the nuclear charge. Equation (2.3) can be written in a more compact way grouping all terms except the nuclear kinetic operator T_{nuc} into the electronic Hamiltonian:

$$\mathscr{H}_F = T_{nuc} + H_{el}. \qquad (2.4)$$

The total wavefunction can be exactly represented as a product of coupled electron and nuclear wavefunctions without making any approximation, through the Born-Huang/Born-Oppenheimer expansion:

$$\Psi(\mathbf{R},\mathbf{r},t) = \sum_j \psi_j'(\mathbf{r})\chi_j'(\mathbf{R},t) = \sum_j \psi_j(\mathbf{r};\mathbf{R})\chi_j(\mathbf{R},t). \qquad (2.5)$$

$\psi_j'(\mathbf{r})$ and $\chi_j'(\mathbf{R},t)$ are the electronic and nuclear wavefunctions in the *diabatic* representation, and $\psi_j(\mathbf{R},\mathbf{r})$ and $\chi_j(\mathbf{R},t)$ are their counterparts in the *adiabatic* representation.

The diabatic wavefunctions do not depend parametrically on the nuclear positions and are typically defined to be orthogonal $\left\langle \psi_j'(\mathbf{r}) \middle| \psi_k'(\mathbf{r}) \right\rangle = \delta_{jk}$. This means that when the diabatic expansion is inserted in (2.1), one can see that the Hamiltonian matrix has only diagonal kinetic energy terms, and both diagonal and non-diagonal potential energy terms. The diagonal elements of the potential

$$H_{jj}(\mathbf{R}) = \left\langle \psi_j'(\mathbf{r}) \middle| H_{el} \middle| \psi_j'(\mathbf{r}) \right\rangle \qquad (2.6)$$

are the $3M$-dimensional diabatic potential energy surfaces (PES), M being the number of atoms.

On the other hand, in the adiabatic representation, the electrons follow the static or time-independent Schrödinger equation

$$H_{el}\psi_j(\mathbf{R},\mathbf{r}) = E_j(\mathbf{R})\psi_j(\mathbf{R},\mathbf{r}), \qquad (2.7)$$

so that $\psi_j(\mathbf{R},\mathbf{r})$ and $E_j(\mathbf{R})$ are the eigenfunctions and eigenvalues of H_{el}, respectively. The adiabatic PES are then the functions $E_j(\mathbf{R})$. Choosing to solve the TDSE in the adiabatic basis is very common because the electronic wavefunctions are naturally orthogonal to each other (since they are eigenfunctions), so that they can directly form a basis. Furthermore, most of the

electronic structure methods are written in the adiabatic basis, so it is convenient. The nuclear wavefunction evolves following the TDSE, which in the adiabatic basis can be expressed as

$$[T_{nuc} + E_i(\mathbf{R})]\chi_i(\mathbf{R},t) + \sum_j V_{i,j}(\mathbf{R})\chi_j(\mathbf{R},t) = i\frac{\partial}{\partial t}\chi_i(\mathbf{R},t). \qquad (2.8)$$

This was obtained by rotating the nuclear kinetic operator into the adiabatic basis, or more explicitly, inserting the Born-Huang/Born-Oppenheimer expansion from (2.5) into (2.2) and multiplying by $\psi_i^*(\mathbf{r};\mathbf{R})$ from the left and then integrating over the electronic degrees of freedom $\mathbf{r}$. As mentioned before, $E_i(\mathbf{R})$ are the adiabatic PES for the ith electronic state and the new term resulting from the rotation, $V_{i,j}(\mathbf{R})$, is the hopping term that allows transitions between the ith and jth PES:

$$V_{i,j}(\mathbf{R}) = -\sum_I \left[\frac{1}{2m_I}G_{i,j}^I(\mathbf{R}) + 2\mathbf{d}_{i,j}^I(\mathbf{R})\cdot\nabla_I\right]. \qquad (2.9)$$

$G_{i,j}^I(\mathbf{R}) = \langle i|\nabla_I^2|j\rangle$ is the scalar coupling vector in the braket notation and

$$\mathbf{d}_{i,j}^I(\mathbf{R}) = \langle i|\nabla_I|j\rangle \qquad (2.10)$$

is the derivative coupling matrix, more often called *nonadiabatic coupling vector* or NAC. It can be determined from the Hellman-Feynman theorem [12–15]:

$$\mathbf{d}_{i,j}^I(\mathbf{R}) = \frac{\langle i|\left[\nabla_I H_{el}(\mathbf{R})\right]|j\rangle - \delta_{i,j}\nabla_I E_i(\mathbf{R})}{E_j(\mathbf{R}) - E_i(\mathbf{R})}. \qquad (2.11)$$

In some limiting cases, the electronic and nuclear degrees of freedom of the total wavefunction can be factorized into a single product. One of these cases is what is called the Born-Oppenheimer approximation [16]. In the adiabatic representation, this is translated into assuming that the NACs can be ignored in (2.8). The expression in (2.11) can give us a hint of when this is a good approximation. For instance, if the energy difference in the denominator is too large (the PES are very far from each other) then the NACs can be neglected. Additionally, the numerator scales as a force term, so if the force on the nuclei is small enough (the nuclei are moving slowly enough compared to the electrons) the NACs play a negligible role.

A visual representation of the full quantum dynamics corresponding the exact solution to a problem beyond the Born-Oppenheimer approximation in the adiabatic representation is shown in figure 2.1.

2.1.2 Mixed Quantum-Classical Dynamics: Non-Adiabatic Molecular Dynamics

In the Born-Oppenheimer approximation, the nuclear wavefunction propagates adiabatically on a single PES. Since this is not a good approximation
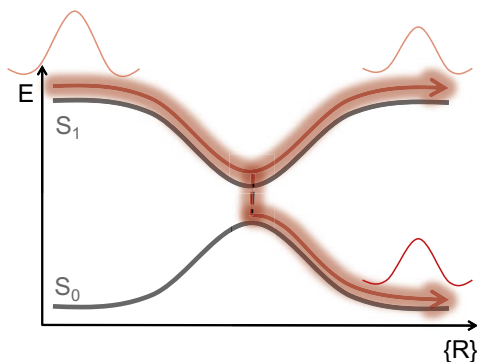
Figure 2.1. Schematic illustration of the full quantum dynamics. The initial wavefunction propagates in the adiabatic excited state PES S_1 and the final wavefunction is a superposition of states in S_1 and the ground state PES S_0 after passing through region with a high NAC. The horizontal axis indicates a general reaction coordinate.

for many time-dependent problems of interest, we need methods that go beyond the Born-Oppenheimer approximation, which is what methods like the ones encompassed in the term Non-Adiabatic Molecular Dynamics (NA-MD) do. Since solving numerically the nuclear TDSE scales exponentially with the dimension of the problem, it is limited to very small molecules of less than 5 atoms. There are several ways of reducing the dimensionality by selecting the important vibrational modes which are relevant for the problem, which can allow for slightly bigger molecules, but approximations need to be made for larger systems.

The mixed quantum-classical dynamics retains the quantum nature of the electrons but makes the approximation that the nuclear degrees of freedom can be described classically. The classical equations of motion scale linearly with dimension (instead of exponentially), which reduces the complexity of the problem substantially. The multiple spawning, and specially Ehrenfest and surface hopping approaches, described in the following subsections, are the most popular mixed quantum-classical methods and have been applied to a very long list of materials and phenomena. More information about these methods can be found in these extensive reviews [17–20].

Ehrenfest dynamics

The Ehrenfest method is a mean field approach that considers that the electronic and nuclear wavefunctions in (2.5) are uncorrelated:

$$\Psi(\mathbf{R},\mathbf{r},t) = \chi_0(\mathbf{R},t)\sum_j c_j(t)\psi_j(\mathbf{R},\mathbf{r}). \qquad (2.12)$$

χ_0 is a single Gaussian function (which is assumed to be highly localized in space) and the $c_j(t)$ are complex coefficients. According to the Ehrenfest

theorem the Newtonian laws are satisfied for mean values in quantum systems with momentum $\mathbf{p}$, mass m and under a potential V:

$$\frac{d\langle\mathbf{r}\rangle}{dt} = \frac{\langle\mathbf{p}\rangle}{m} \quad \text{and} \quad \frac{d\langle\mathbf{p}\rangle}{dt} = \langle\nabla V\rangle. \tag{2.13}$$

By using the Ehrenfest theorem and making the local approximation of H_{el} one arrives to the equations of motion for the time-dependent nuclear quantities, positions $\mathbf{R}$ and momenta $\mathbf{P}$:

$$\frac{\partial\mathbf{R}}{\partial t} = \langle\Psi|\,i\,[H_{el},\mathbf{R}]\,|\Psi\rangle = \frac{\mathbf{P}}{M}$$
$$\frac{\partial\mathbf{P}}{\partial t} = \langle\Psi|\,i\,[H_{el},-i\nabla]\,|\Psi\rangle = \langle\Psi|\,\nabla H_{el}(\mathbf{R})\,|\Psi\rangle. \tag{2.14}$$

$[A,B]$ is the commutator of A and B, and M is the mass of the nucleus. In summary, in Ehrenfest dynamics the nuclei move in a single average PES, as figure 2.2 shows.
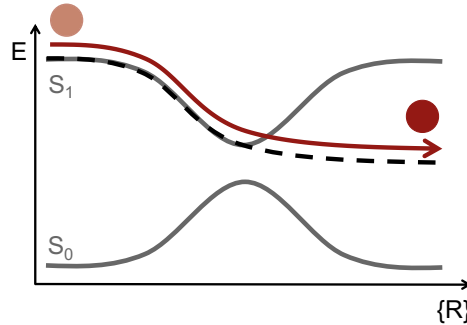
Figure 2.2. Schematic illustration of the Ehrenfest dynamics. Trajectories run on a mean field PES averaged over all the electronic states, weighted by their electronic population. The horizontal axis indicates a general reaction coordinate.

It is interesting to note that the forces on the nuclei are averaged over many adiabatic electronic states influenced by the nuclear motion and have the following form:

$$F_{\text{Ehrenfest}} = \frac{\partial}{\partial r}\langle\Psi|\,H_{\text{el}}\,|\Psi\rangle. \tag{2.15}$$

This expression should not be confused with the Hellman-Feynman forces that are calculated in ground state methods

$$F_{\text{GS}} = \left\langle\Psi\left|\frac{\partial}{\partial r}H_{\text{el}}\right|\Psi\right\rangle, \tag{2.16}$$

17

where the partial derivative can be moved inside the expectation value because it is a stationary case, unlike in (2.15).

One of the major assumptions taken in this method is that the nuclear wavefunction can be represented by a single Gaussian function, instead of a sum of Gaussians or more accurate functions. This, combined with the classical treatment of the trajectory, results in branching of the wavefunction not being possible, which would be allowed if the nuclear degrees of freedom were treated fully quantum mechanically. Furthermore, this method is overcoherent, which means that it is unable to describe the decoherence of electronic states, resulting in long-lived electronic excitations. However, Ehrenfest dynamics is able to appropriately describe systems in which the nuclei are heavy and the range of motion is small, and the electron-nuclear correlations are minimal. It has been successfully applied to nanostructures, big molecules and other extended systems to study processes that do not conserve energy.

Surface Hopping

In order to have a better description of the electron-nuclear correlation in Eherenfest dynamics, Tully developed a surface hopping (SH) scheme based on Molecular Dynamics (MD) [21]. In this family of methods, the nuclear trajectory evolves in a single adiabatic electronic PES but is allowed to hop to another surface, which is dictated by a probability, as figure 2.3 shows. The main idea behind SH methods is to approximately recover the quantum behaviour of the nuclear trajectories by calculating multiple events of the same trajectory, which, given the randomness included in the probability, generate different outcomes.

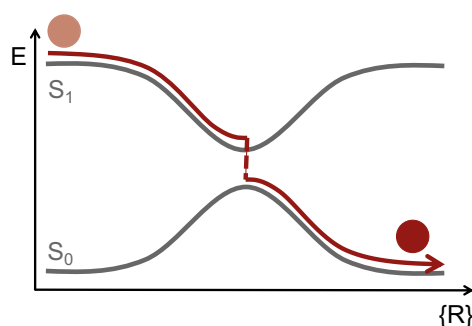*Figure 2.3.* Schematic illustration of the SH methods. An ensemble of trajectories are propagated on the adiabatic BO PES and jumps are allowed between them. The horizontal axis indicates a general reaction coordinate.

The most broadly used SH method is the *Fewest Switches Surface Hopping* (FSSH), in which the population balance is maintained with the minimum amount of hops possible. In its most popular implementation, the nu-

clear system is treated classically via *ab initio* MD and the electronic wave-function $\psi(\mathbf{r}, \mathbf{R}, t)$ is represented in the basis of adiabatic electronic functions $\phi(\mathbf{r}; \mathbf{R}(t))$. They can be taken as Kohn-Sham (KS) orbitals if DFT is the method of choice, as in the following expression:

$$\psi(\mathbf{r}, \mathbf{R}, t) = \sum_i c_i(t) \phi_i(\mathbf{r}; \mathbf{R}(t)). \tag{2.17}$$

The c_i are the time-dependent expansion coefficients, and their evolution is governed by a TDSE, which can be expressed as follows:

$$i \frac{\mathrm{d} c_i}{\mathrm{d} t} = \sum_j \left(\varepsilon_i \delta_{ij} - i \mathbf{d}_{ij} \right) c_j. \tag{2.18}$$

ε_i is the diagonal part of the electron Hamiltonian and the off-diagonal $\mathbf{d}_{ij}$ represent the NAC have already been defined in (2.10). The probability for the transition from an electronic state $|i\rangle$ to a new state $|j\rangle$ in a small time interval $\Delta t = t = t'$ can be expressed as

$$g_{i \rightarrow j}(t) = \max \left(0, P_{i \rightarrow j}(t) \right) \tag{2.19}$$

with

$$P_{i \rightarrow j}(t) \approx 2 \frac{\mathrm{Re} \left[c_i^*(t') c_j(t') \frac{\mathbf{P}}{M} \mathbf{d}_{ij}(t) \right]}{c_i^*(t') c_j(t')}. \tag{2.20}$$

These probabilities are compared to a uniformly distributed random number to determine if the system is to remain in the current PES or hop to the next one and nuclear velocities are rescaled to maintain the total energy. If that rescaling is not possible then the hop is rejected.

In the original FSSH, the nuclear and electronic degrees of freedom are completely coupled, so everything is updated on the fly at each time step. However, the Classical Path Approximation (CPA) [22] can be used to further reduce the computational cost by making the approximation that the classical trajectory of the nuclei is independent of the electronic dynamics but the electronic dynamics still depends on the nuclear positions. In practice, this means that the electronic problem can be solved on a series of pre-computed nuclear trajectories, typically from *ab initio* MD. Since the feedback from the electrons is not taken into account, this approximation is not valid if the electron-nuclear correlations are crucial, such as in small systems like molecules. However, it is expected to produce reasonably good results for extended solids and it is currently the most widespread method to tackle solid-state systems. In FSSH-CPA, the hop rejection and velocity rescaling from (2.19) become

$$g_{i \rightarrow j}(t) \longrightarrow g_{i \rightarrow j}(t) b_{i \rightarrow j}(t), \tag{2.21}$$

where the probability is scaled by a Boltzmann factor to account for the fact that transitions to states high up in energy are less probable:

$$b_{i \to j}(t) \begin{cases} \exp\left(-\frac{E_j - E_i - \hbar\omega}{k_B T}\right) & \text{if } E_j > E_i + \hbar\omega \\ 1 & \text{if } E_j \leq E_i + \hbar\omega. \end{cases} \qquad (2.22)$$

Here k_B is the Boltzmann constant, T is the temperature, and $\hbar\omega$ is the energy of the absorbed photon in case of light-matter interaction, where $\hbar$ has been included for clarity.

Same as with Ehrenfest dynamics, by having a classical description of the nuclei, we miss the loss of quantum coherence within the electronic subsystem that is induced by the interaction with the quantum-mechanical vibrations. Surface hopping can develop non-physical coherences and this is why *decoherence-induced surface hopping* (DISH) was developed. It accounts for the branching of nuclear trajectories by allowing hops at the decoherence times only, which are calculated within the optical response theory using the autocorrelation function of the fluctuation of the energy gap between two electron states, as described in [23].

Multiple Spawning

In the last MQCD method that I will discuss here, the Multiple Spawning (MS) method, the nuclear wavefunctions are expanded as a linear combination of Gaussian functions that are propagated classically. It is common to refer to it as *ab initio* Multiple Spawning when it is connected to an electronic structure method. The main difference between MS and the previously described methods is that the number of nuclear functions is not a constant, and each function is allowed to bifurcate and produce two functions in regions of the PES landscape in which the NACs are large, as figure 2.4 shows. These are called spawning events and give name to the method.

In the theoretical case of an infinite basis, the MS is an exact theory, in opposition to both SH and Ehrenfest dynamics. However, since the NACs need to be calculated at each time step and the basis of the nuclear functions can be large, MS is computationally very expensive. Therefore, compromises need to be made to truncate the basis as well as making local approximations to compute integrals, which reduces the applicability of MS on large systems or long timescales, in favour of less accurate but more practical methods like Ehrenfest or SH.

2.2 The electronic system

So far I have discussed how to treat the coupling between the electronic and ionic degrees of freedom. In this chapter I will focus on the quantum-mechanical approach to the electronic system, introducing an effective density framework
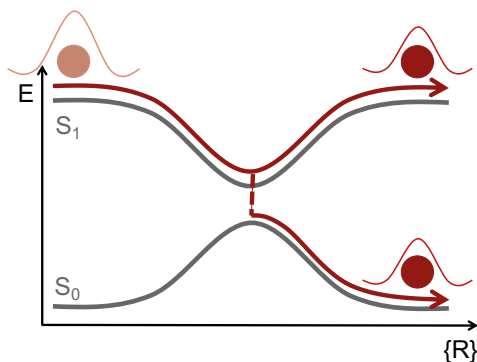
Figure 2.4. Schematic illustration of the MS method. Classical trajectories are represented by single Gaussian functions. After the high NAC region, multiple Gaussians can be created in different PES than the original. The horizontal axis indicates a general reaction coordinate.

that reduces the degrees of freedom of the problem making it tractable. I will first describe the general time-dependent case with Time-Dependent Density Functional Theory (TDDFT) and then I will consider the special case of time-independent or ground state Density Functional Theory (DFT).

2.2.1 Time-Dependent Density Functional Theory

I will start by assuming that the electronic system is non-adiabatic. We can think about approaching the problem directly by solving the time-dependent Schrödinger equation, but this is even more difficult than for the ground state (which I will develop in 2.2.2) and it becomes extremely computationally expensive as the number of electron grows. However, inspired by ground state DFT, we can try to develop a time-dependent DFT in order to reduce the number of variables in our problem. We will see in this section that Runge and Gross proved the time-dependent equivalent of the KS theorem and I will give an overview on the basics of TDDFT.

One-to-one correspondence and Time-Dependent Kohn-Sham equations
The evolution of the wavefunction describing N interacting electrons is given by the time-dependent Schrödinger equation, which I have already shown in (2.1) but choose to include here for clarity:

$$i\frac{\partial \Psi(\mathbf{R},\mathbf{r},t)}{\partial t} = \mathscr{H}\Psi(\mathbf{R},\mathbf{r},t). \tag{2.23}$$

Since it is a first-order differential equation in time, it needs an initial condition from the wavefunction at time 0 ($\Psi(t=0)$). The Hamiltonian operator is

$$\mathscr{H} = T_e + V_{e-e} + V_{ext}(t), \tag{2.24}$$

21

where I have now grouped in $V_{ext}(t)$ the potential the electrons experience due to the nuclear attraction as well as any external potential applied to the system. In general, it is a sum over all the electrons

$$V_{ext} = \sum_{i=1}^{N} v_{ext}(\mathbf{r}_i, t). \tag{2.25}$$

The electron density (normalized to the number of electrons N) is given by

$$n(\mathbf{r}, t) = N \int d^3\mathbf{r}_2 \ldots \int d^3\mathbf{r}_N |\Psi(\mathbf{r}_1, \mathbf{r}_2 \ldots \mathbf{r}_N, t)|^2 \tag{2.26}$$

and evolves with time from an initial point $t = 0$. Runge and Gross proved an analog of the Hohenberg-Kohn theorem for time-dependent systems in what is called the one-to-one correspondence [24]. This theorem, central in TDDFT, states that the densities $n(\mathbf{r}, t)$ and $n'(\mathbf{r}, t)$ evolving from the same initial state $\Psi(t = 0)$ under the influence of two potentials $v_{ext}(\mathbf{r}, t)$ and $v'_{ext}(\mathbf{r}, t)$ that are Taylor expandable around $t = 0$ will eventually differ if the potentials differ by more than a purely time-dependent function:

$$\Delta v_{ext}(\mathbf{r}, t) = v_{ext}(\mathbf{r}, t) - v'_{ext}(\mathbf{r}, t) \neq c(t). \tag{2.27}$$

What this means is that there is a one-to-one correspondence between one-electron densities and potentials. This implies that we only need to know the time-dependent density of a system evolving from a given initial state to uniquely identify the potential that produced that density. The potential in its turn completely determines the Hamiltonian, so (2.23) can be solved to obtain all the properties of the system.

Now, knowing that finding functionals of the density is a difficult task, I will turn to the Kohn-Sham system, a fictitious system of non-interacting electrons that reproduce the density of the interacting electrons. All the real properties can be obtained from the effective density of the KS system, which is time-dependent:

$$n_{eff}(\mathbf{r}, t) = \sum_{j=1}^{N} |\phi_j(\mathbf{r}, t)|^2. \tag{2.28}$$

The KS orbitals ϕ evolve according to the time-dependent KS equation:

$$i\frac{\partial}{\partial t}\phi_j(\mathbf{r}, t) = \left[-\frac{\nabla^2}{2} + v_{KS}\left[n_{eff}; \psi(0)\right](\mathbf{r}, t) \right] \phi_j(\mathbf{r}, t). \tag{2.29}$$

This v_{KS} (parametrically dependent on the initial state) is unique and can be decomposed in three terms:

$$v_{KS}\left[n_{eff}; \Psi\right](\mathbf{r}, t) = v_{ext}(\mathbf{r}, t) + v_H(\mathbf{r}, t) + v_{xc}(\mathbf{r}, t). \tag{2.30}$$

$v_H(\mathbf{r},t)$ is the usual Hartree potential and the exchange-correlation potential $v_{xc}(\mathbf{r},t)$ is a very complicated quantity, even more than in the ground state because it is a functional of the entire history of the density, the initial interacting wavefunction $\psi(0)$ and the initial KS wavefunction $\phi(0)$. In ground state DFT, the exchange-correlation potential is the functional derivative of the exchange-correlation energy, which is not so simple in TDDFT. A first attempt to deal with time-dependent exchange-correlation functionals is to use the Adiabatic Local Density Approximation (ALDA), even if it neglects all nonlocality in time. More sophisticated functionals with memory effects have been proposed [25–27].

Response functions and time-propagation in TDDFT

Many interesting physical quantities are the reaction of a system to an external perturbation and can be expressed as a response function. More explicitly, if an external field F is applied to a many-electron system, the system responds and this can be measured as a change in a physical observable P as a functional of F:

$$\Delta P = \Delta P_F[F]. \tag{2.31}$$

Its exact form can be very complex, but if F is weak, the response can be written as a power series of the field strength. The first order response is called the linear response of the observable. For example, the first order response of the dipole moment to an external electric field is the polarizability and the first order response of a magnetic moment to a homogeneous magnetic field is the magnetic susceptibility.

There are different methods to calculate response functions from TDDFT: real time propagation (RT-TDDFT), Sternheimer [28, 29], and Cassida methods [30]. Here I am going to focus on the first one, which consists of propagating the electronic density in real time according to the TD-KS equation in (2.29) using the so-called *adiabatic approximation*. Therefore, the KS Hamiltonian is a functional of the instantaneous density, not the whole history. If no perturbation is present, the evolution of the KS wavefunction is

$$\phi_j(t) = \phi_j(0)\mathrm{e}^{-i\varepsilon_j(0)t}, \tag{2.32}$$

where ε_j is the eigenvalue of the jth KS wavefunction. However, if there is an applied time-dependent perturbation with a frequency ω and a strength λ of the general form

$$v_{ext}(\mathbf{r},t) = \lambda(\mathbf{r})\cos(\omega t) + \lambda(\mathbf{r})\sin(\omega t), \tag{2.33}$$

then we can obtain the evolution of the wavefunctions from (2.29) and thus all the response functions. For instance, we can calculate the dielectric properties of our systems with RT-TDDFT by studying its dynamical response to the perturbation created by a weak external electric field by monitoring the evolution

of the electrical dipole moment $p_{j,k}$, which is calculated through

$$p_{j,k}(t) = \text{Tr}\left[\mathbf{D}^k n(t)\right], \qquad (2.34)$$

where j and k indicate the directions of the applied field and measurement respectively, and the transition dipole tensor operator is defined as

$$\mathbf{D}^k_{\mu\nu} = \langle \varphi_\mu | \hat{e}_k \cdot \mathbf{r} | \varphi_\nu \rangle, \qquad (2.35)$$

where φ are the basis functions in the electronic structure method of choice. $\mathbf{D}$ is related to the polarizability tensor $\alpha(t)$ by

$$p_{j,k}(t) = \int_{-\infty}^{t} \alpha_{j,k}(t-t')E_j(t')dt', \qquad (2.36)$$

with E_j being the jth spatial component of the external electric field. If we apply an instantaneous delta pulse

$$E(t) = E_0\delta(t-t_0)\hat{e}_j, \qquad (2.37)$$

it yields the following after Fourier transforming:

$$\alpha_{j,k}(\omega) = \frac{p_{j,k}(\omega)}{E_0}. \qquad (2.38)$$

The absorption cross section can be obtained via

$$\sigma_{j,k}(\omega) = \frac{4\pi\omega}{c}\text{Im}\left[\alpha_{j,k}(\omega)\right], \qquad (2.39)$$

which leads to the optical absorption spectra (strength function)

$$S(\omega) = \frac{1}{3}\text{Tr}\left[\sigma(\omega)\right]. \qquad (2.40)$$

In RT-TDDFT higher-order responses (hyperpolarizabilities) are included. The linear response regime can be achieved by applying a weak enough electric field, as the nonlinear contributions to the response function will be negligible. This capability of RT-TDDFT to explore phenomena that go beyond the first, second or third order in perturbation theory result in it being a great tool to study phenomena such as *High Harmonic Generation* (HHG). HHG is the process by which a target system is illuminated with a laser frequency of a certain frequency ω and it emits light in frequencies that are multiples of ω (harmonics), as figure 2.5 presents.

HHG is relatively well understood for atoms and small molecules [31, 32], but its fundamentals are still under discussion for extended systems such as solids, monolayers and large molecules [33–37]. Many theoretical studies rely on perturbation theory and therefore are limited to the second or third
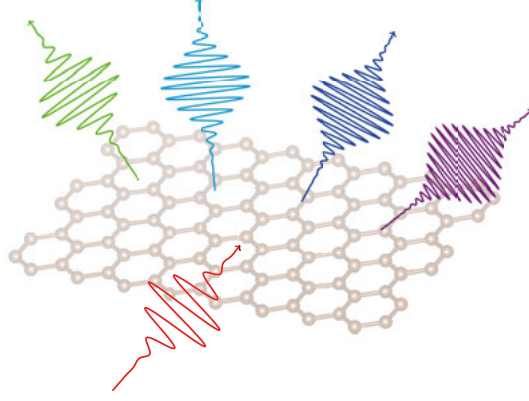
Figure 2.5. Schematic illustration of the high harmonic generation in a graphene flake. The red wave indicates the incoming laser, the outgoing waves are the high harmonics generated by the target.

harmonic order [38], and the few that use RT-TDDFT, although they report a good matching with experiments, are quite inconclusive in terms of giving an explanation for the mechanisms behind the phenomenon [39–41].

There is currently a discussion whether the spectral function $S(\omega)$ is proportional to the dipole, its velocity or its acceleration. It has been shown that for an atomic system, the HHG response is proportional to the dipole velocity [42]:

$$S(\omega) = \frac{1}{4\varepsilon_0^2 c^2} |\dot{p}(\omega)|^2.$$

(2.41)

Therefore, because RT-TDDFT provides the dipole in the time domain, the HHG spectra is calculated as the following Fourier transform of its velocity:

$$\text{HHG}_{j,k}(\omega) \propto \text{FT}\left[\left|\dot{p}_{j,k}(t)\right|^2\right].$$

(2.42)

2.2.2 Density Functional Theory

I will now consider a special case: if the time-dependence of the ionic system influences the electronic system only through the Born-Oppenheimer approximation and there are no external fields that give a time dependency to the Hamiltonian, then the first order differential equation (TDSE) can have a time-independent solution multiplied by an integrating factor that carries the time-dependency. This is exactly what the Born-Oppenheimer approximation means in practice, that we can solve the electronic problem in each snapshot of frozen ions. Therefore, we can focus on the time-independent part of the problem and discuss Density Functional Theory (DFT).

With all these considerations, the wavefunction can be written as a simple product of time-dependent and time-independent parts, which leads to the time-independent Schrödinger equation:

$$\mathscr{H}\Psi(\mathbf{r}_1, \mathbf{r}_2, ...\mathbf{r}_N, \mathbf{R}_1, \mathbf{R}_2, ...) = E\Psi(\mathbf{r}_1, \mathbf{r}_2, ...\mathbf{r}_N, \mathbf{R}_1, \mathbf{R}_2, ...). \qquad (2.43)$$

Equation (2.43) can only be solved exactly for the case of the hydrogen atom, and approximations need to be introduced already for the helium atom, which has 3 particles. If we restrict ourselves to stationary or ground state properties, the already introduced Born-Oppenheimer approximation can be used relying on the fact that the ions are much heavier than electrons and therefore can be considered as *frozen*, so that they become a static term in the external potential that the electrons feel. Within the BO approximation, the electronic Hamiltonian has a simpler expression:

$$\mathscr{H} = -\frac{1}{2}\sum_i \nabla_i^2 - \sum_{i,I} \frac{Z_I}{|\mathbf{r}_i - \mathbf{R}_I|} + \frac{1}{2}\sum_{i \neq j} \frac{1}{|\mathbf{r}_i - \mathbf{r}_j|}. \qquad (2.44)$$

Even with this approximation, a many-body equation for a system of N interacting particles needs to be solved. The first simplification came with the introduction of the Thomas-Fermi-Dirac approximation [43–45], when the many-body wavefunction was substituted by the electron density n of the system. The foundations of DFT were established on this approximation, from which follows that electronic properties can be calculated using $n(\mathbf{r})$ and that the total energy of the system is a functional of this density, $E[n(\mathbf{r})]$.

The formulation of DFT is based on the two Hohenberg-Kohn theorems [46], which shift the attention from the ground state many-body wavefunction to the one-body electron density, a function of only three variables and thus more manageable. The theorems are:

Theorem 1. *For any problem of interacting particles in an external potential $V_{ext}(\mathbf{r})$, there exists a one-to-one correspondence, except for a constant, between this potential and the ground state electronic density $n_0(\mathbf{r})$.*

Theorem 2. *For any applied external potential in an interacting many-body system, the total energy can be written as a functional of the density. Then, the exact ground state electronic density is the one that minimizes the total energy functional.*

Once we solve the eigenvalue problem, the full many-body wavefunction (from which all other properties can be calculated) is completely determined, because the Hamiltonian is known, except for a shift in energy. This is not possible for realistic systems due to the size of the variable space. The first theorem implies that this can be achieved through the ground state electronic

density, from which the wavefunction can be calculated. However, it does not specify how to get the ground state density, which is what the second theorem states. This second theorem means that any property of an interacting system can be obtained from the ground state electron density $n_0(\mathbf{r})$ via the minimization of the total energy functional, now $E[n_0(\mathbf{r})]$.

The Kohn-Sham ansatz

Even if these theorems state that the many-body problem can be solved via the density, they do not provide an expression of the total energy as a function of this density. For that we turn to the Kohn-Sham (KS) formalism [47], which has the task of finding an auxiliary non-interacting system (having the non-interacting part of the kinetical energy) exposed to an effective potential V_{eff} that results in the same density that the interacting system with an external potential V_{ext} has. The non-interacting system has the effective Hamiltonian

$$\mathscr{H}_{eff} = -\frac{1}{2}\nabla^2 + V_{eff}(\mathbf{r}), \tag{2.45}$$

and the effective density can be calculated in terms of the single-electron KS orbitals ϕ

$$n_{eff}(\mathbf{r}) = \sum_{i=1}^{N} |\phi_i(\mathbf{r})|^2. \tag{2.46}$$

The kinetic energy is given by

$$T_{eff} = -\frac{1}{2}\sum_{i=1}^{N} \langle \phi_i | \nabla^2 | \phi_i \rangle, \tag{2.47}$$

and the classical Coulomb energy of the electron density interacting with itself (or Hartree energy) is defined as

$$E_{Hartree} = -\frac{1}{2}\int d\mathbf{r}d\mathbf{r}' \frac{n_{eff}(\mathbf{r})n_{eff}(\mathbf{r}')}{|\mathbf{r}-\mathbf{r}'|}. \tag{2.48}$$

The Kohn-Sham ansatz replaces the Hohenberg-Kohn ground state energy functional with

$$E_{KS} = T_{eff} + \int d\mathbf{r} V_{ext}(\mathbf{r})n_{eff}(\mathbf{r}) + E_{Hartree}[n_{eff}] + E_{xc}[n_{eff}], \tag{2.49}$$

where V_{ext} is any external potential including the one due to the nuclei. The many-body effects of exchange and correlation are grouped into the exchange-correlation energy E_{xc}.

The Kohn-Sham equations

The ground state of (2.49) is found by minimizing the energy with respect to the ϕ using Lagrange multipliers, which results into the Schrödinger-like KS equation:

$$\mathcal{H}_{eff}(\mathbf{r})\phi_i(\mathbf{r}) = \left[-\frac{1}{2}\nabla^2 + V_{eff}(\mathbf{r})\right]\phi_i = \varepsilon_i\phi_i(\mathbf{r}). \qquad (2.50)$$

V_{eff} includes the potential due to the nuclei, the Hartree potential and the exchange-correlation potential $V_{xc} = \dfrac{\delta E_{xc}[n_{eff}]}{\delta n_{eff}[\mathbf{r}]}$. Solving the KS equation in a self-consistent way yields the eigenvalues ε_i, which are not unique and have no physical meaning [48]. However, the total energy that can be calculated from the KS orbitals is a physical quantity:

$$E = \sum_{i=1}^{N}\varepsilon_i - \frac{1}{2}\int d\mathbf{r}d\mathbf{r}'\frac{n_{eff}(\mathbf{r})n_{eff}(\mathbf{r}')}{|\mathbf{r}-\mathbf{r}'|} - \int d\mathbf{r}V_{xc}(\mathbf{r})n_{eff}(\mathbf{r}) + E_{xc}[n_{eff}].$$
$$(2.51)$$

The Exchange-Correlation functional

The explicit form of the exchange-correlation functional is unknown so we must make approximations to it. Just to mention some, the Local Density Approximation (LDA) and the Generalized-Gradient Approximation (GGA) are introduced next.

In the Local Density Approximation (LDA) [46,47] the exchange-correlation energy is fitted to that of a uniform electron gas, where electrons move on a positively charged background distribution so that the local ensemble is electrically neutral. This is translated into the form

$$E_{xc}^{LDA}[n] = \int n(\mathbf{r})\varepsilon_{xc}[n(\mathbf{r})]d\mathbf{r}, \qquad (2.52)$$

where ε_{xc} is the exchange-correlation energy per particle of a uniform electron gas with density n and can be separated into two terms:

$$\varepsilon_{xc}[n(\mathbf{r})] = \varepsilon_x[n(\mathbf{r})] + \varepsilon_c[n(\mathbf{r})]. \qquad (2.53)$$

The first term is commonly taken as the Slater exchange and has an analytic form, but there is no exact expression for the correlation part. However, various ε_{xc} have been constructed based on highly accurate numerical quantum Monte Carlo calculations.

In an attempt of improving the agreement with experimental results, the Generalized Gradient Approximation (GGA) [49] considers not only the density at a certain point but also its gradient, including the non homogeneity of the true electron density:

$$E_{xc}^{GGA}[n(\mathbf{r})] = \int n(\mathbf{r})\varepsilon_{xc}[n(\mathbf{r}), \nabla n(\mathbf{r})]d\mathbf{r}. \qquad (2.54)$$

ε_{xc} can also be separated into the exchange and the correlation parts. Both LDA and GGA can easily be generalized to include spin polarization in the calculations.

2.2.3 Periodicity, basis sets and pseudopotentials

We have been able to replace the solution of a many-body Schrödinger equation for an interacting system using the complete wavefunction by self-consistently solving the non-interacting KS equation expressed in a chosen basis. In this thesis I am going to describe two different basis sets: plane waves (PW) and numerical atomic orbitals (NAO).

Before that, I am going to assume that we are working in a periodic system, which mathematically means that any function describing it obeys the Born-von Karman boundary conditions. In an ideal infinite solid, the number of electrons is also infinite, but this can be overcome due to the fact that it is a crystal, thus periodic (if impurities and defects are neglected). V_{eff} in (2.50) can be chosen to have the periodicity of the underlying Bravais lattice, so $V_{eff}(\mathbf{r}+\mathbf{R}) = V_{eff}(\mathbf{r})$, where $\mathbf{R}$ is a translation lattice vector.

Bloch's theorem [50] states that the eigenstates ψ of the one-electron Hamiltonian $H = -\frac{1}{2}\nabla^2 + V_{eff}(\mathbf{r})$, where $V_{eff}(\mathbf{r}+\mathbf{R}) = V_{eff}(\mathbf{r})$ for all $\mathbf{R}$ in a Bravais lattice, can be chosen to have the form of a plane wave times a function with the periodicity of the Bravais lattice as

$$\psi_{n\mathbf{k}} = e^{i\mathbf{k}\cdot\mathbf{r}}u_{n\mathbf{k}}(\mathbf{r}), \tag{2.55}$$

for which $u_{n\mathbf{k}}(\mathbf{r}+\mathbf{R}) = u_{n\mathbf{k}}(\mathbf{r})$. Exploiting the periodicity of $u_{n\mathbf{k}}$, it can be expressed in a Fourier series:

$$u_{n\mathbf{k}}(\mathbf{r}) = \sum_{\mathbf{G}} c_{n,\mathbf{G}} e^{i\mathbf{G}\cdot\mathbf{r}}. \tag{2.56}$$

$\mathbf{G}$ is the reciprocal lattice vector and the $c_{n,\mathbf{G}}$ are plane wave expansion coefficients. Thus, any periodic wavefunction can be expanded in a set of plane waves with the periodicity of the lattice:

$$\psi_{n,\mathbf{k}} = \sum_{\mathbf{G}} c_{n,\mathbf{k}+\mathbf{G}} e^{i(\mathbf{k}+\mathbf{G})\cdot\mathbf{r}}. \tag{2.57}$$

Therefore, the problem of having an infinite number of electrons has been solved because the number of $\mathbf{k}$ points needed to calculate the electronic properties is a finite number and can be limited to the irreducible Brillouin zone. However, the sum in (2.57) has infinite number of terms and can not be performed computationally. Consequently, the series must be truncated at a cutoff value $|\mathbf{G}|$ (corresponding also to a cutoff energy), which introduces an error. The cutoff has to be chosen as a compromise of the computational effort and the accuracy of the calculation.

It needs to be mentioned that a periodic implementation is not only limited to infinite bulk solids. The concept of the *supercell* was introduced to extend it to systems that break the periodicity, such as semi-infinite systems (surfaces, two-dimensional materials, ribbons, wires...), as well as systems with defects.

However, the implementation of the single-particle KS equation is still not an easy task, since the electronic wavefunctions behave very differently in different regions of space. Near the core region they oscillate wildly while they are basically free-electron like in the valence region, so a complete basis that is able to capture these behaviors is needed. There are several possible choices and some are better suited than others for specific tasks. In this thesis I am going to focus on plane waves (PW) as implemented in the Quantum Espresso [51, 52] and VASP [53–55] codes, and numerical atomic orbitals (NAO) as in the SIESTA software [56].

Plane waves

Using a basis set of plane waves has a very strong advantage since it is relatively easy to develop and implement methods based on k-space representation, where operations such as derivatives and Fast Fourier transforms can be performed almost effortlessly. Furthermore, plane waves are the solution of the Schrödinger equation of a free particle and, although this is not the case of the electrons in solids where nuclei and electrons interact strongly via the Coulomb potential, the Fermi Liquid theory shows that excitations near the Fermi level in metals can be treated as independent quasi-particles [50].

Using plane waves for the valence electrons wavefunctions far from the nuclei is justified, but they fail to describe the electrons inside the core radius r_c. They are strongly bound and oscillate heavily because they adopt the form of the atomic wavefunctions. Also, the valence wavefunctions oscillate in the core region due to orthogonality. Trying to expand such wiggling functions would require an enormous amount of plane waves, which is computationally not feasible. A way to overcome this challenge is to use a pseudopotential [57], a new softer potential V_{pseudo} acting only on the valence electrons and which is identical to the real potential outside of the problematic region. Additionally, its ground state wavefunction ψ_{pseudo} is equal to the all electron wavefunction but nodeless in the core region (see fig. 2.6). With this, the core states and the nodes of the valence wavefunctions in the core region are removed. Therefore, ψ_{pseudo} varies smoothly and can be represented with a low number of plane waves. By doing this frozen core approximation some information is lost and core electrons can not be studied. However, in most of the applications the region of interest is $r > r_c$, where chemical bonding happens.

Numerical Atomic Orbitals (NAO)

The use of pseudopotentials is not strictly necessary with atomic basis sets, but it is convenient to get rid of the core electrons and to have a smooth charge density that can be expanded in a spatial grid. NAOs are strictly confined
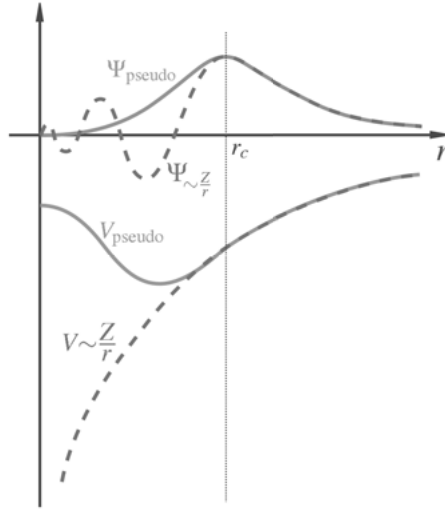
Figure 2.6. Sketch of the actual Coulomb potential and wavefunctions (dashed line), compared to the softer pseudopotential and the nodeless pseudofunction related to it (solid line). The real and pseudo-functions are the same beyond the core radius r_c. From [58].

atomic orbitals, which means that they are zero beyond a certain radius. Inside said radius, they are products of a numerical radial function and spherical harmonics, which, for an atom I sitting in $\mathbf{R}_I$ have the following form:

$$\varphi_{Ilmn} = \varphi_{Iln}(r_I)Y_{lm}(\hat{r}_I). \tag{2.58}$$

The angular momentum (l, m) can be arbitrarily large and there will be different orbitals (n) with the same angular momentum but different radial dependence (multiple ζ basis). For example, the minimal single-ζ (SZ) basis set has one radial function per angular momentum, a double-ζ has two and so on. More details on this can be found in [56].

2.3 Non-equilibrium kinetic theory

2.3.1 Phonons

Atoms in a crystalline lattice vibrate around their equilibrium positions with an amplitude that depends on the temperature. The vibrations can be studied as collective modes corresponding to excitations of the lattice, which are called phonons. Phonons are bosonic particles and their bosonic states can be populated, just like electronic ones. Each vibrational mode that composes a phonon excitation corresponds to an energy (or a vibration frequency), and the group of energies associated with each vibrational mode form the phonon spectra or phonon band structure, as it is often visualized in reciprocal space. Because

phonons represent ionic vibrations, understanding phonon spectra is important for multiple phenomena that rely on the crystalline lattice vibrations, such as superconductivity or thermal conductivity.

The potential energy Φ of the phonon system can be written as a Taylor expansion in terms of the deviations of each ionic position from its equilibrium, or atomic displacements u:

$$\Phi = \Phi_0 + \sum_{l\kappa}\sum_{\alpha}\Phi_\alpha(l\kappa)u_\alpha(l\kappa) + \frac{1}{2}\sum_{ll'\kappa\kappa'}\sum_{\alpha\beta}\Phi_{\alpha\beta}(l\kappa,l'\kappa')u_\alpha(l\kappa)u_\beta(l'\kappa') +$$

$$\frac{1}{3!}\sum_{ll'l''\kappa\kappa'\kappa''}\sum_{\alpha\beta\gamma}\Phi_{\alpha\beta\gamma}(l\kappa,l'\kappa',l''\kappa'')u_\alpha(l\kappa)u_\beta(l'\kappa')u_\gamma(l''\kappa'') + \dots. \quad (2.59)$$

l is the label of unit cell, κ are the atoms in each unit cell, and α, β and γ are the Cartesian coordinates. The expansion coefficients Φ_0, Φ_α, $\Phi_{\alpha\beta}$ and $\Phi_{\alpha\beta\gamma}$ are the 0th, 1st, 2nd and 3rd order force constants respectively. If the displacements are small, the problem can be solved up to 2nd order in the harmonic approximation, and the higher order terms can be treated within perturbation theory.

The second order force constant matrix has elements given by

$$\Phi_{\alpha\beta}(l\kappa,l'\kappa') = \frac{\partial^2\Phi}{\partial u_\alpha(l\kappa)u_\beta(l'\kappa')} = -\frac{\partial F_\beta(l'\kappa')}{\partial u_\alpha(l\kappa)}, \quad (2.60)$$

where F_β are the ionic forces in the Cartesian direction β.

The phonon spectrum can be obtained by solving the following eigenvalue problem:

$$D(\mathbf{q})\mathbf{e}_{\mathbf{q}j} = \omega_{\mathbf{q}j}^2\mathbf{e}_{\mathbf{q}j}. \quad (2.61)$$

The dynamical matrix is

$$D_{\kappa\kappa'}^{\alpha\beta} = \sum_{l'}\frac{\Phi_{\alpha\beta}(0\kappa,l'\kappa')}{\sqrt{m_\kappa m_{\kappa'}}}\exp^{i\mathbf{q}\cdot[\mathbf{r}(l'\kappa')-\mathbf{r}(0\kappa)]}, \quad (2.62)$$

where $\mathbf{r}$ are the equilibrium positions, $\mathbf{q}$ is the wave vector, j is the branch index, $\omega_{\mathbf{q}j}$ is the phonon frequency and $\mathbf{e}_{\mathbf{q}j}$ is the polarization vector of the phonon mode labeled by $\{\mathbf{q}, j\}$. By solving (2.61), the phonon spectrum or band structure and the density of states can be calculated.

Once the phonon spectrum is known, the total energy of the phonon system can be calculated in the canonical distribution

$$E_{ph} = \sum_{\mathbf{q}j}\hbar\omega_{\mathbf{q}j}\left[\frac{1}{2} + \frac{1}{\exp(\hbar\omega_{\mathbf{q}j}/k_BT) - 1}\right], \quad (2.63)$$

where I have included $\hbar$ for clarity, k_B is the Boltzman constant and T stands for temperature. All other thermodynamic quantities such as heat capacity, entropy and Helmholtz free energy can be calculated from the energy.

In order to calculate the lattice thermal conductivity for solids at temperatures around room temperature we need to go beyond the harmonic approximation, since it is governed by phonon-phonon scattering. To achieve good agreement with experimental results it is necessary to include third order force constants in our calculations, which are used to compute the imaginary part of the self-energy, as reported in [59].

The fourth term in (2.59) can be expressed as a sum of three-phonon collisions in terms of creation a_λ and annihilation operators $a_\lambda^\dagger$:

$$\Phi_3 = \sum_{\lambda \lambda' \lambda''} \Phi_{\lambda \lambda' \lambda''} (\hat{a}_\lambda + \hat{a}_{-\lambda}^\dagger)(\hat{a}_{\lambda'} + \hat{a}_{-\lambda'}^\dagger)(\hat{a}_{\lambda''} + \hat{a}_{-\lambda''}^\dagger). \tag{2.64}$$

λ and $-\lambda$ are a short-hand notation for the phonon modes $(\mathbf{q}, j)$ and $(-\mathbf{q}, j)$, respectively. The imaginary part of the self-energy is then calculated from (2.64) to second order using many-body perturbation theory and is related to the phonon linewidths. The phonon lifetime of mode λ can be calculated as an inverse of its linewidth:

$$\tau_\lambda = \frac{1}{2\gamma_\lambda(\omega_\lambda)}. \tag{2.65}$$

Finally, the lattice thermal conductivity is written as

$$\kappa = \frac{1}{NV_0} \sum_\lambda C_\lambda \mathbf{v}_\lambda \otimes \mathbf{v}_\lambda \tau_\lambda, \tag{2.66}$$

where N is the number of phonon modes, V_0 is the volume of the unit cell, C_λ is the mode-dependent heat capacity, and $\mathbf{v}_\lambda$ is the group velocity.

In practice, within the DFT formalism we can calculate the force constants using finite differences of the total energy with respect to atomic displacements in a supercell, as it is described in [59, 60].

The third order force constant is

$$\Phi_{\alpha\beta\gamma}(l\kappa, l'\kappa', l''\kappa'') = \frac{\partial^3 \Phi}{\partial u_\alpha(l\kappa) u_\beta(l'\kappa') u_\gamma(l''\kappa'')}, \tag{2.67}$$

and in this framework it can be obtained as

$$\Phi_{\alpha\beta\gamma}(l\kappa, l'\kappa', l''\kappa'') \simeq -\frac{F_\gamma[l''\kappa''; \mathbf{u}(l\kappa)\mathbf{u}(l'\kappa')]}{u_\alpha(l\kappa) u_\beta(l'\kappa')}, \tag{2.68}$$

with $F_\gamma[l''\kappa'']$ as the atomic force measured at position $\mathbf{r}(l''\kappa'')$ under a pair of displacements $\mathbf{u}(l\kappa)$ and $\mathbf{u}(l\kappa')$. The harmonic force constant in (2.60) can be similarly approximated as

$$\Phi_{\alpha\beta}(l\kappa, l'\kappa') \simeq -\frac{F_\beta[l'\kappa'; \mathbf{u}(l\kappa)]}{u_\alpha(l\kappa)}, \tag{2.69}$$

where $F_\beta[l'\kappa'; \mathbf{u}(l\kappa)]$ is the atomic force measured at position $\mathbf{r}(l'\kappa')$ under a displacement $\mathbf{u}(l\kappa)$.

2.3.2 Rate equations

In this section I am going to introduce a theory that describes the energy exchange between two systems in contact, which in our case will be the phonon and the electronic systems. The two temperature model will set the foundations for the more advanced development that includes phonon-phonon interactions.

Two temperature model

I start by discussing the two-temperature model (2TM), which is often used to describe the out of equilibrium dynamics of the energy transfer between two systems that are in contact, typically after a laser excitation. I will consider these two systems to be the lattice, which I will describe in terms of phonons, and the electrons, and will follow the derivation in [61].

The 2TM assumes the two subsystems to be internally and separately in equilibrium and connected by the electron-phonon coupling. Furthermore, it is based on energy conservation: the energy that the laser introduces into the system goes primarily to the electrons, which then transfer it to the phonons, so that the change in time of the electronic energy E_e must be equal to the negative change in time of the lattice energy E_l:

$$\frac{\partial E_e}{\partial t} = -\frac{\partial E_l}{\partial t}.$$ (2.70)

The lattice, as I have mentioned, can be described in terms of phonons, so that the lattice energy is given by

$$E_l = \sum_Q \hbar \omega_Q n_Q,$$ (2.71)

where Q stands for a combination of the phonon branch index ν and reciprocal space vector $\mathbf{q}$, ω_Q are the phonon frequencies, and n_Q is the phonon population. The electronic energy is in its turn expressed in terms of the electron Bloch energy ε_k and the electron population f_k as

$$E_e = 2 \sum_k \varepsilon_k f_k,$$ (2.72)

with k being short hand notation for the electron band index n and the reciprocal space vector $\mathbf{k}$. Since I assume the electronic system to be in equilibrium, f_k can be taken as a Fermi-Dirac distribution with temperature $T_e(t)$

$$f_k(t) = \frac{1}{e^{\frac{\varepsilon_k - \varepsilon_F(T_e)}{k_B T_e(t)}} + 1},$$ (2.73)

with ε_F being the chemical potential or Fermi energy and k_B the Boltzmann constant. The phononic system is also in equilibrium at the lattice temperature

$T_l(t)$, and since they are bosinc particles, their population can be taken as a Bose-Einstein distribution:

$$n_Q(t) = \frac{1}{e^{\frac{\hbar\omega_Q}{K_B T_l(t)}} - 1}. \tag{2.74}$$

The 2TM assumes that the distribution functions change in time only due to electron-phonon scattering. Fermi's golden rule for scattering theory can be used to obtain the exact expressions for $\dot{f}_k$ and $\dot{n}_Q$, also known as the Bloch-Boltzmann-Peierls formulas [62]:

$$\dot{f}_k = \dot{f}_k|_{e-ph}^{scatt.} =$$
$$-\frac{2\pi}{\hbar} \sum_Q |M_{kk'}|^2 \{ f_k(1-f_{k'}) [(n_Q+1)\delta(\varepsilon_k - \varepsilon_{k'} - \hbar\omega_Q) + n_Q\delta(\varepsilon_k - \varepsilon_{k'} + \hbar\omega_Q)]$$
$$- (1-f_k)f_{k'} [(n_Q+1)\delta(\varepsilon_k - \varepsilon_{k'} + \hbar\omega_Q) + n_Q\delta(\varepsilon_k - \varepsilon_{k'} - \hbar\omega_Q)] \} \tag{2.75}$$

and

$$\dot{n}_Q = \dot{n}_Q|_{e-ph}^{scatt.} =$$
$$-\frac{4\pi}{\hbar} \sum_k |M_{kk'}|^2 f_k(1-f_{k'}) [n_Q\delta(\varepsilon_k - \varepsilon_{k'} + \hbar\omega_Q) - (n_Q+1)\delta(\varepsilon_k - \varepsilon_{k'} - \hbar\omega_Q)]. \tag{2.76}$$

$M_{kk'}$ is the electron-phonon scattering matrix element, and I have considered all first order the Feynman diagrams for electron-phonon scattering only. In this step, the perturbation given by the electron-phonon coupling has been considered to be small. Further conditions for this step to be valid are that the system is Markovian and that it can be described by individual partition functions, so that correlations are ignored.

Using the conservation of energy (2.70) becomes

$$2\sum_k \dot{f}_k|_{e-ph}^{scatt.} + \sum_Q \hbar\omega_Q\dot{n}_Q|_{e-ph}^{scatt.} = 0. \tag{2.77}$$

Now making the approximation that temperatures are small and we can focus on energies around the Fermi energy, we can write

$$\frac{\partial E_e}{\partial t} = 2\sum_k \dot{f}_k|_{e-ph}^{scatt.} = -\sum_Q \hbar\omega_Q\dot{n}_Q|_{e-ph}^{scatt.} =$$
$$\sum_Q \gamma_Q \int_{-\infty}^{\infty} d\varepsilon \int_{-\infty}^{\infty} d\varepsilon' [(f_{k'} - f_k)n_Q - f_k(1-f_{k'}]\delta(-\varepsilon_k + \varepsilon_{k'} + \hbar\omega_Q), \tag{2.78}$$

with γ_Q the phonon linewidth. Performing a Taylor expansion around T_e for (2.73) and introducing the lattice and electronic specific heats C_l and C_e, re-

spectively, we obtain the final rate equations that define the 2TM

$$C_e \frac{\partial T_e}{\partial t} = -G(T_e - T_l), \qquad (2.79a)$$

$$C_l \frac{\partial T_l}{\partial t} = G(T_e - T_l), \qquad (2.79b)$$

with $G = \sum_Q \gamma_Q C_Q$ and C_Q the phonon mode-dependent specific heat.

Introducing phonon-phonon interactions

The 2TM does not consider phonon-phonon scattering, but it can be included (see figure 2.7) to have a more accurate description of the phonon population dynamics.
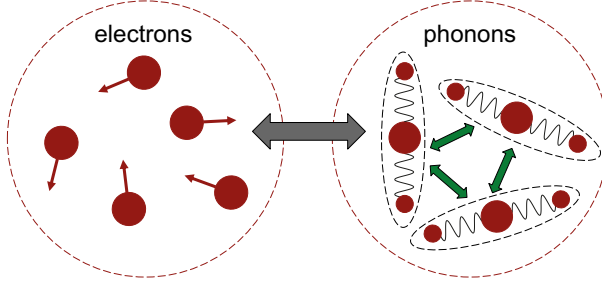

Figure 2.7. Treatment of the electron-phonon dynamics. The 2TM model describes the transfer between the electronic and phononic systems as a whole (gray arrow). When phonon-phonon interactions are included, energy transfer between the phononic subsystems is also considered (green arrows).

In this section I will arrive at an analogue of the rate equations in (2.79), following a similar derivation to the one I followed in the previous section. I will consider 3-body processes, so that two phonons scatter into one or viceversa. By considering these contributions in the scattering Fermi Golden Rule, new terms appear in $\dot{n}_Q$

$$\dot{n}_Q|_{ph-ph}^{scatt.} = -\frac{2\pi}{\hbar} \sum_{kk'} |\Phi_{Qkk'}|^2 [(n_Q+1)(n_k+1)n_{k'}\delta(\omega_Q + \omega_k - \omega_{k'}) +$$

$$(n_Q+1)(n_{k'}+1)n_k\delta(\omega_Q + \omega_{k'} - \omega_k) - n_Q n_k(n_{k'}+1)\delta(\omega_Q - \omega_{k'} + \omega_k) -$$
$$n_Q n_{k'}(n_k+1)\delta(\omega_Q + \omega_{k'} - \omega_k) + (n_Q+1)n_k n_{k'}\delta(\omega_Q - \omega_{k'} - \omega_k) -$$
$$n_Q(n_k+1)(n_{k'}+1)\delta(\omega_Q - \omega_{k'} - \omega_k)], \qquad (2.80)$$

where $\Phi_{Qkk'}$ is the anharmonic force constant. By defining the phonon linewidth due to phonon-phonon scattering Γ_{Qk}, assuming $T_l^k \approx T_l^{k'}$ and introducing $T^{kk'} = \frac{2T_l^{k'}T_l^k}{T_l^{k'}+T_l^k}$, I arrive to the following expression after Taylor expanding

36

around small temperature changes:

$$\dot{n}_Q|_{ph-ph}^{scatt.} = \sum_k \Gamma_{Qk} C_Q (T_l^Q - T_l^{kk'}). \tag{2.81}$$

T_l^Q is the temperature of each phonon branch. This expression determines the changes of phonon population due to phonon-phonon interaction and it depends on the phonon mode and branch.

Combining this with the terms given by the electron-phonon interaction that I considered in the 2TM I reach to the analogous rate equations:

$$C_Q \frac{\partial T_l^Q}{\partial t} = -G_Q (T_l^Q - T_e) \left[1 + J(\omega_Q, T_l^Q)(T_l^Q - T_e) \right] - \sum_{k'} \Gamma_{Qk'} C_Q (T_l^Q - T_l^{k'}), \tag{2.82a}$$

$$C_e \frac{\partial T_e}{\partial t} = \sum_Q G_Q (T_l^Q - T_e) \left[1 + J(\omega_Q, T_l^Q)(T_l^Q - T_e) \right]. \tag{2.82b}$$

Comparison to experiments: diffuse scattering

X-Ray diffuse scattering (DS) is an experimental technique that measures the inelastic scattering caused by lattice vibrations, phonons (see figure 2.8). In a scattering experiment, phonons that are scattered elastically form sharp peaks in the reciprocal space, called Bragg peaks. DS is the background signal that appears between Bragg peaks as well, and can be used to determine phonon dispersion relations. The DS scattering in reciprocal space can be written as [63]

$$I(\mathbf{q}) \propto \sum_v \frac{1}{\omega_v(\mathbf{q})} \left[n_v(\mathbf{q}) + \frac{1}{2} \right] |F_v(\mathbf{q})|^2, \tag{2.83}$$

where $\omega_v(\mathbf{q})$ is the frequency of a phonon with mode v and wave vector $\mathbf{q}$, $n_v(\mathbf{q})$ is the phonon occupancy number and $F_v(\mathbf{q})$ is the structure factor. An example of an experimental and theoretical work where this has been studied can be found in [64].
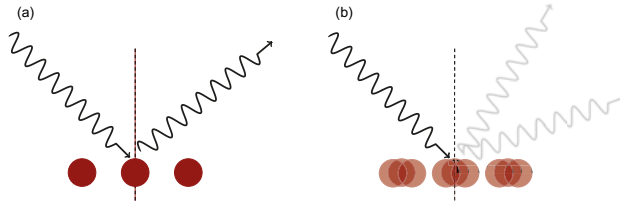

Figure 2.8. (a) Elastic scattering producing Bragg peaks, (b) diffuse scattering due to lattice vibrations.

3. Defect and interface induced phenomena in monolayer MoS$_2$

This chapter summarizes the results of Papers I and II. Two-dimensional (2D) transition dichalcogenides, and specially MoS$_2$ have been extensively investigated due to their multiple applications as candidates to substitute silicon in electronic devices [65,66]. Although mechanical and chemical exfoliation are nowadays standard techniques to obtain 2D MoS$_2$ from bulk samples, these monolayers are not perfect. Multiple defects have been reported to appear, as well as different phases of the material coexisting in one single sample [67]. Studying the implications of these deviations from a perfect MoS$_2$ monolayer is extremely important in order to be able to understand the properties of realistic samples. We have approached this challenge in two different ways. In Paper I we investigated the effect of point defects on the electron-hole recombination in the most stable phase of MoS$_2$, using time-dependent *ab initio* non-adiabatic molecular dynamics. This is relevant because charge recombination is one of the most important phenomena hindering charge separation, the basic principle of solar cells. In Paper II we studied the coexistence of several phases of monolayer MoS$_2$ focusing on the effect of geometric reconstructions, which happen near and far from the interfaces, has on the electronic properties of the compound samples, using density functional theory.

3.1 Summary of Paper I: Charge recombination

Even if we theoreticians often think about perfect solids and surfaces, the truth is that experimental samples have finite size effects and often defects. In paper I we studied how point defects affect electron-hole recombination times using NA-MD, in particular FSSH (see section 2.1.2 for the theoretical description). As we have mentioned, charge recombination is one of the main channels

for energy and carrier losses that reduce the material's efficiency. Therefore, understanding these phenomena in more realistic samples is the path towards going from research to industrial applications.

3.1.1 Ground state properties

We used DFT to obtain ground-state properties like atomic positions and eigenvalues. Since we introduced defects, we needed to consider supercells that were large enough to avoid interaction between the defects and their periodic images. Furthermore, monolayer MoS_2 is a direct band gap semiconductor and its conduction band minimum (CBM) and valence band maximum (VBM) are located at the K high-symmetry point of the Brillouin zone. We used Γ-point calculations, and in order to achieve correct band-folding of the K point to Γ, the size of the supercell needs to be commensurate with the coordinates of K. That means supercell sizes need to be multiples of 3, and we chose $6 \times 6 \times 1$ as a compromise between computational efficiency and accuracy.

We studied S vacancy (vac-S), S interstitial (int-S), Mo vacancy (vac-Mo) and Mo interstitial (int-Mo), which are shown in figure 3.1. We identified the energy levels that correspond to the CBM and VBM in pristine by visualizing their charge densities. The CBM are completely undistorted in all the defected systems, but the VBM in int-S and vac-Mo is slightly distorted by out of plane components of the charge density. This is shown in figure 3.2 and we will see that it has an effect in the recombination dynamics.

3.1.2 Non-adiabatic dynamics: electron-hole recombination

We performed the NA dynamics calculations by following the methodology introduced in section 2.1.2. For each system we selected the energy levels that can participate in the recombination in order to form the *active space* in which the DISH algorithm will be applied. Some eigenvalues are degenerate and we needed to consider all the possible transitions between them. For instance, in the pristine system the VBM and CBM are doubly degenerate so the active space is formed by 4 orbitals and we considered excited states corresponding to the CBM $\rightarrow$ VBM transition, where the depopulation of the excited state is expected to decay to the ground state. To obtain the recombination timescale τ we fitted the population increase in the ground state with an exponential function of the form

$$P(t) = 1 - \exp\left(\frac{-t}{\tau}\right), \tag{3.1}$$

so that it reaches the normalized value of 1 at infinite time. In the defected systems, the mid gap defect levels introduce alternative recombination mechanisms to the direct one, and all the intermediate transitions need to be considered. A scheme of the active space and possible transitions is shown in
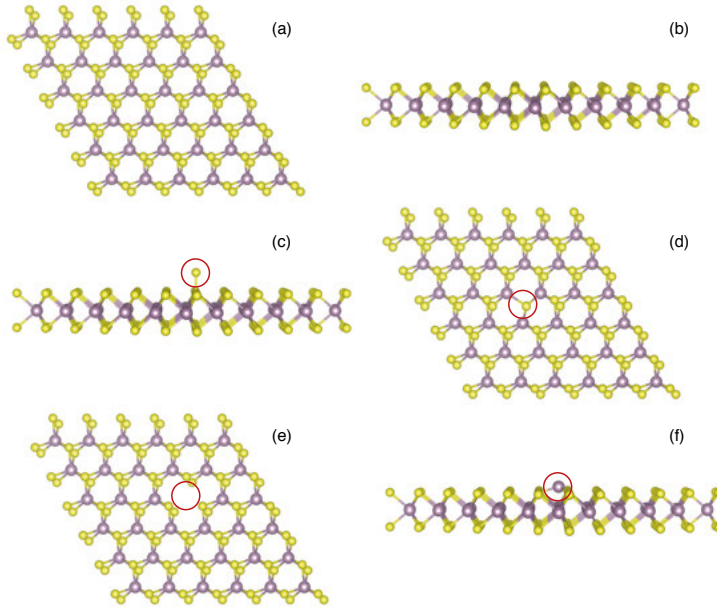
Figure 3.1. Supercells of the studied MoS$_2$ systems. S atoms are represented in yellow and Mo atoms in violet. (a) and (b) show top and side views of the pristine supercell respectively. (c-f) show the defected structures with the defect site marked with a red circle. (c) is int-S, (d) is vac-S, (e) is vac-Mo and (f) is int-Mo. Reproduced with permission from Paper I.
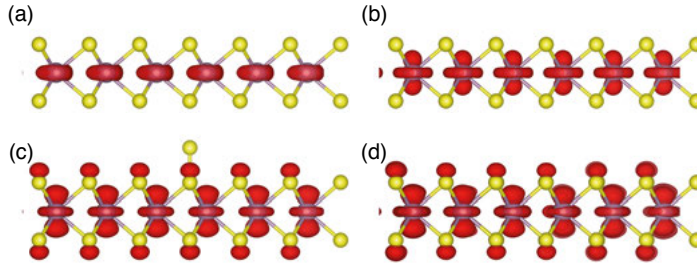

Figure 3.2. In red, charge density of pristine VBM (a), pristine CBM (b), and the distorted VBMs in int-S (c) and vac-Mo (d).

figure 3.3. Unoccupied defect levels (dashed green lines) act as electron traps because excited electrons coming from the CBM can fall in these defect levels before recombining with the holes in the VBM. In the same way, occupied defect states (dashed red lines) act as hole traps.

We consider all the transitions with all the intermediate steps and the over-all recombination time is calculated as the fastest of all the combinations, a summary of which is shown in table 3.1. The details of the intermediate tran-
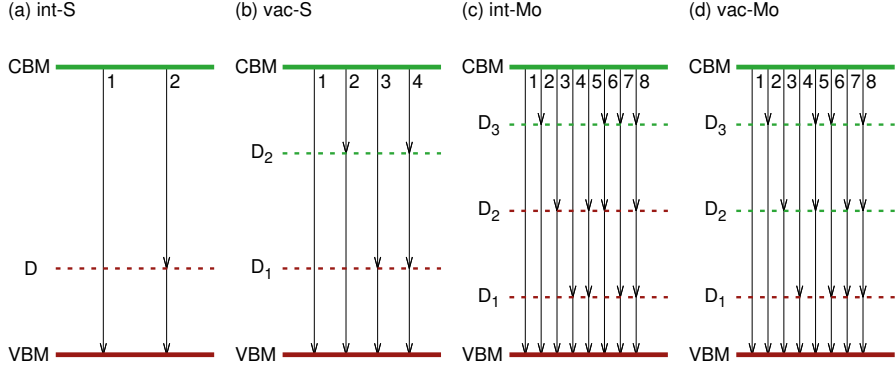
Figure 3.3. Scheme of the active space and possible transitions in (a) int-S, (b) vac-S, (c) int-Mo and (d) vac-Mo. Red and green lines indicate occupied and unoccupied levels, respectively. Defect states inside the gap are shown with a dashed line.

Table 3.1. *Summary of the fastest pathways in each of the studied systems. The numbers in parentheses are related to the transitions in Figure 3.3. Reproduced with permission from Paper I.*

System	Processes
pristine	Direct (1)
int-S	Hole trap (2)
vac-S	Electron trap (2)
int-Mo	Hole trap 1 (3), double hole trap (5), electron and hole traps 1 (6)
vac-Mo	Hole trap (4), and hole and electron traps 1 (6)

sitions (timescales and active space) for all the studied systems are included in the paper.

We found out that all direct recombination times are affected by the presence of defects, which results in an acceleration of the timescales. This is more noticeable in the systems whose CBM is more distorted, int-S and vac-Mo (see figure 3.2), which have a direct recombination time that is 1/3 and 1/2 of the pristine one, respectively. However, for the defected systems, there is always an alternative mechanism involving a defect state that is faster than the direct recombination.

Our results match qualitatively with experiments, although in order to match quantitatively we would need to go beyond the single-particle picture to include the excitonic effects that MoS_2 shows, which are known to accelerate the recombination dynamics [68, 69]. However, since we studied the lowest lying excited states, this has been shown to be a fair approximation [68, 70].

We have observed that the results are very sensitive to many simulation parameters in the method, and are going to discuss some of them here. As mentioned before, we chose to include decoherence via DISH, but this is not the only method available. We performed a test in which decoherence was treated within the simplified decay of mixing (SDM) [71], which is an energy-based decoherence correction. We found that our timescales changed rather drastically when using SDM instead of DISH, as table 3.2 shows. It is not clear which scheme is better in general, as both include decoherence in an *ad hoc* manner, and therefore further studies are required. We did several tests to understand what the inclusion of more energy levels in the active space would do, and we concluded that this has a rather weak effect. This is also included in table 3.2.

Table 3.2. *Effect on the active space and decoherence scheme to the non-radiative electron-hole recombination time in pristine MoS$_2$.*

Active space size	Decoherence scheme	τ
4 (2 in VBM, 2 in CBM)	DISH	70 ns
5 (3 in VBM, 2 in CBM)	DISH	50 ns
5 (3 in VBM, 2 in CBM)	SDM	300 ps

Furthermore, the computational method that we used does not enforce that the wavefunctions have the same phase at consecutive time steps, needed for NAC calculations. This influenced the quality of our results, as it has been pointed out in [72]. The phase inconsistency has been addressed in a recent development of Libra [73]. Regarding the carrier density, having single-electron excitations in a 6×6×1 supercell produces a carrier concentration of 2.75×10^{13} cm^{-2}, which is higher than present in experiments but lower to the one in previous studies [74, 75], which partially explains our disagreement. Additionally, the 5×5×1 supercell considered in [74, 75] might not be able to capture the K point due to band folding, which means that different vertical transitions were considered.

3.1.3 Conclusions of Paper I

In this paper we presented how the recombination rates and pathways in MoS$_2$ are affected in presence of defects using NA-MD. While the method is very promising and one of the few available options to study the phenomena studied in the paper, certain improvements should be addressed. However, the reported description of the alternative recombination mechanisms introduced by different kind of defects can still be useful to understand the problem in a qualitative way.

3.2 Summary of Paper II: Coexistence of different phases

Two dimensional transition metal dichalcogenides are known to exist in several different phases. In particular, chemically exfoliated MoS_2 is known to have a semiconductor ground state phase (1H) and several metastable polymorphs that have a controversial electronic structure, with experiments claiming metallic, semimetallic and small-gaped semiconductor phases. A recent survey on the topic can be found in [67]. The difficulty to study these metastable phases in experiments arises because they appear as small patches in a majority of ground state 1H phase, and obtaining information about pure metastable phases is beyond the experimental resolution. Often the reported conclusions are the result of indirect observations. Of course, the theoretical route has been explored as well, although the vast majority of the studies treat the pure isolated phases. In Paper II we studied the effect of the coexistence of the ground state phase 1H with the two lowest energy metastable phases: 1T and 1T′, using DFT.

3.2.1 Effect of strain in the band structures of the pure phases

As mentioned before, the ground state of monolayer MoS_2 is a semiconductor with a direct gap of 1.8 eV at the high symmetry point K [76]. This phase, called 1H is formed by sandwiching a Mo atom between two S atoms in an A-B-A stacking, so that S atoms are on top of each other and six S atoms are bonded to the central Mo atom in a trigonal coordination, as figure 3.4 (left) shows. Its band structure is shown in figure 3.5 (a). Higher energy polymorphs are very common as small patches inside the 1H matrix and have an A-B-C stacking with octahedral coordination of S atoms around the central Mo. The 1T phase, which is dynamically unstable, is shown in the center panel of figure 3.4. It is formed by a gliding displacement of one of the S planes in 1H. The 1T′ phase, which is the lowest energy metastable state, appears after the 1T undergoes a Jahn-Teller distortion via the dimerization of the Mo atoms, as it can be seen in the right panel of the same figure.

There is consensus on the fact that the 1T phase is metallic, as the band structure in figure 3.5 (b) shows. The controversy is in whether the 1T′ has a small gap or is semimetallic. We found that it is a semimetal with bands crossing at only one reciprocal point in the Brillouin zone, at the lattice parameter that minimizes the total energy. However, as these two metastable polymorphs are found as patches in the 1H matrix, they are subjected to a planar compressive strain that affects their electronic properties. Since the 1H and 1T lattice parameters are very similar, the strain that the 1T patches feels is very small, which explains why their band structure is not significantly changed. However, due to their larger lattice mismatch, the compressive strain that 1T′ feels when placed in the 1H matrix is enough to open up a small gap.
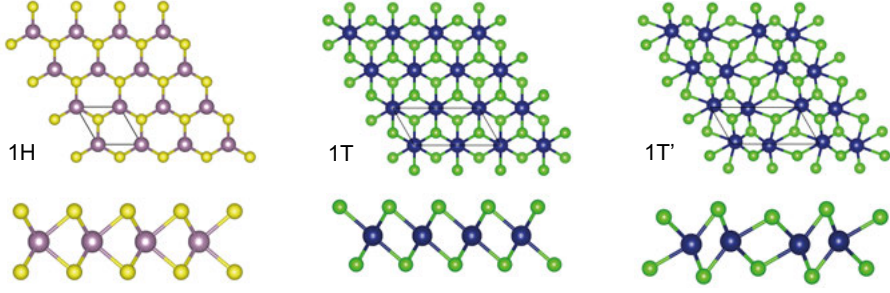
Figure 3.4. Three different phases of monolayer MoS_2: the ground state trigonal 1H and the two octahedral polytopes, 1T and 1T'. Mo atoms are shown in purple in 1H and blue in 1T and 1T', while S atoms are yellow in 1H and green in 1T and 1T'. Different colors have been used to distinguish the mixed phase structures in the discussion.
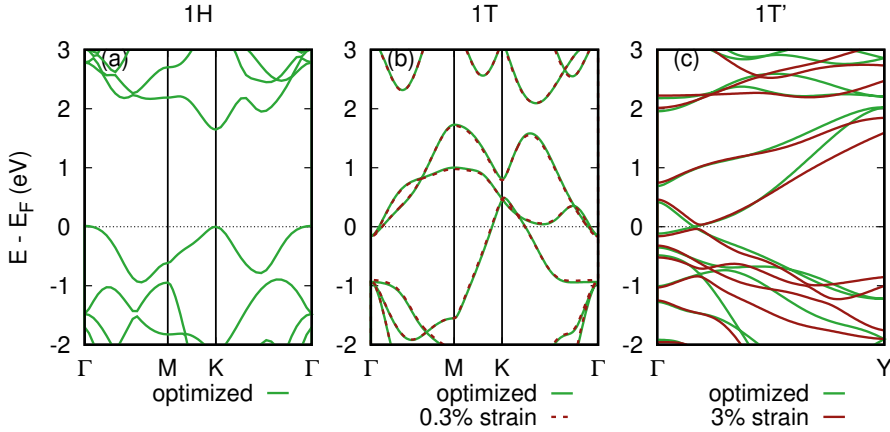

Figure 3.5. Electronic band structure of the studied phases of MoS_2. (a) 1H MoS_2 in its optimized (equilibrium) lattice parameter. (b) and (c) show the effect of strain on the band structure of the octahedral phases: Band structure of 1T (b) and 1T' (c). The green solid line represents the band structure of the cell that minimizes the total energy with respect to the variation of the lattice parameter in each of the phases. The dashed (solid) red line depicts the band structure of the 1T (1T') under the strain that the 1H equilibrium lattice parameter imposes.

3.2.2 Mixed phases: electronic structure

We constructed mixed phases supercells of the ground state 1H as a matrix and a patch of one of the two octahedral polymorphs (1T or 1T'). We considered three different sizes of the supercells but kept the spatial region of 1H between the periodic images constant. The structures were named 1H-1P $X-Y$, 1P being the octahedral phase type (1T or 1T') that we start with, X being the size

of the 1H supercell matrix, and Y being the size of the octahedral phase patch, in units of a hexagonal 1×1 unit cell. An example is represented in figure 3.6.
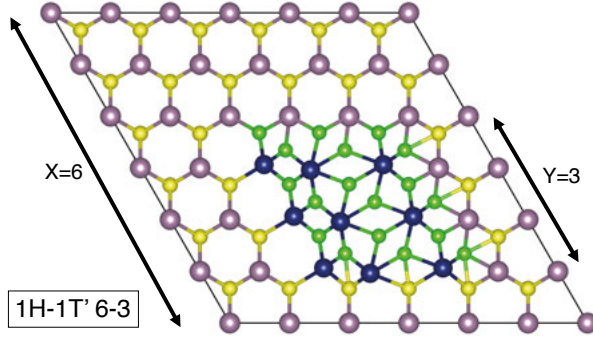

Figure 3.6. An example of a supercell containing two phases: the 1H matrix is a 6×6 supercell, making $X = 6$, and the octahedral patch is 3×3, so that $Y = 3$. Since the patch is in this case 1T′, this structure is named $1H - 1T'$ 6-3.

We performed geometry relaxation in each of these structures in order to minimize the total energy in each case. We observed large structural reconstructions, which will be discussed in the following section, so that the final structures are not composed of the perfect pure phases they started with. The results of this energy minimization are summarized in table 3.3, where we can see the lowest energy structure for each size, together with the gap in brackets. We found that 6-3 and 12-9 1H-1T have lower energy than their 1H-1T′ counterparts, but it is the other way around for size 9-6.

	1H-1T	1H-1T′
6-3	**-770.40** (84)	-770.01
9-6	-1729.82	**-1730.08** (167)
12-9	**-3070.11** (85)	-3068.48

Table 3.3. *Total energies (in eV) and values of the gap of the mixed phases. Bold indicates the lowest energy structure of each size, which opens up a gap, included in parenthesis (in meV). Reproduced with permission from Paper II.*

When plotting the density of states of these systems (figure 3.7), we observed a gap opening for the structures that have lower energy, while the high energy ones from each size remain metallic. There are two interesting points to make here: the gap opening occurs only after relaxation, and, even if the states that are closer to the gap belong to atoms from the interstitial region and to the patch, their wavefunctions are very far from being localized.
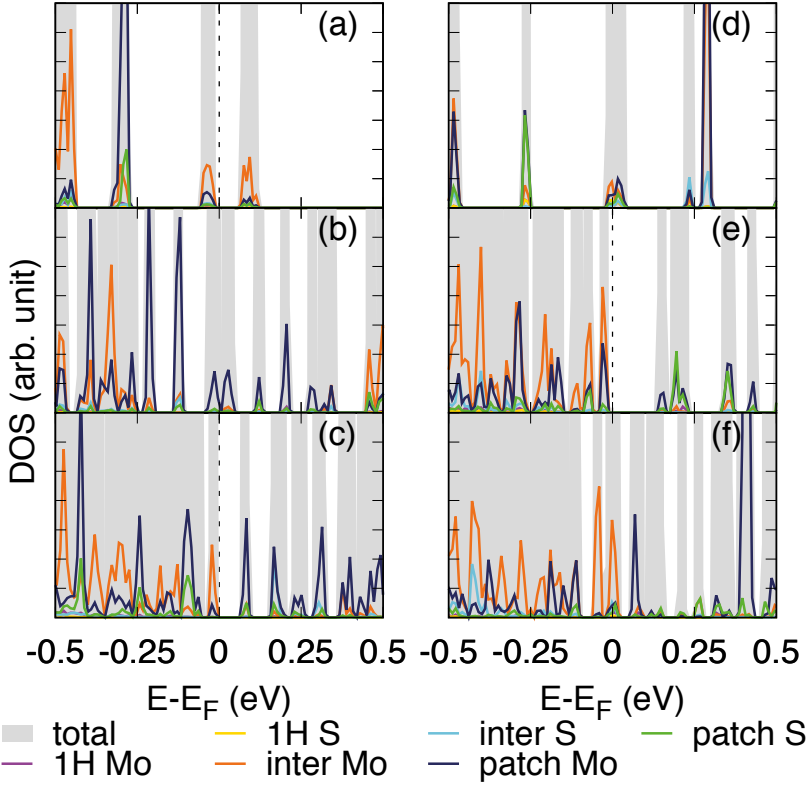
Figure 3.7. Contribution to each atomic type to the DOS of the six structures close to the Fermi energy. (a), (b) and (c) represent the 1H-1T 6-3, 9-6 and 12-9 composites, respectively. Panels (d), (e) and (f) represent the 1H-1T′ 6-3, 9-6 and 12-9 composites, respectively. The gray filled curves are the peaks from the total DOS of each structure, and the solid lines are the partial DOS of selected Mo and S atoms belonging to bulk 1H (purple and yellow, respectively), the interfacial region (orange and light blue, respectively) and the bulk region of the patch, either 1T for the left panel or 1T′ for the right one (dark blue and green). Gap opening happens for (a), (c) and (e). Reproduced with permission from Paper II.

3.2.3 Mixed phases: structural reconstruction

As mentioned before, all the electronic structure changes are due to a large structural distortion after geometric relaxation, which we observed not to be limited to the boundary between the phases. Figures 3.8 and 3.9 present the details for the lowest energy structures, which show a gap opening.

The final atomic positions and bonds are overimposed to the starting ones, shown in grey, and show a clear displacement of the atoms. This differences are larger for the cells that started with a 1T patch, compared to the starting 1T′ patches. We observed large reconstructions in the corner atoms, specially S, as highlighted in figure 3.8 (e) and (f) for 1H-1T, but also present in 1H-
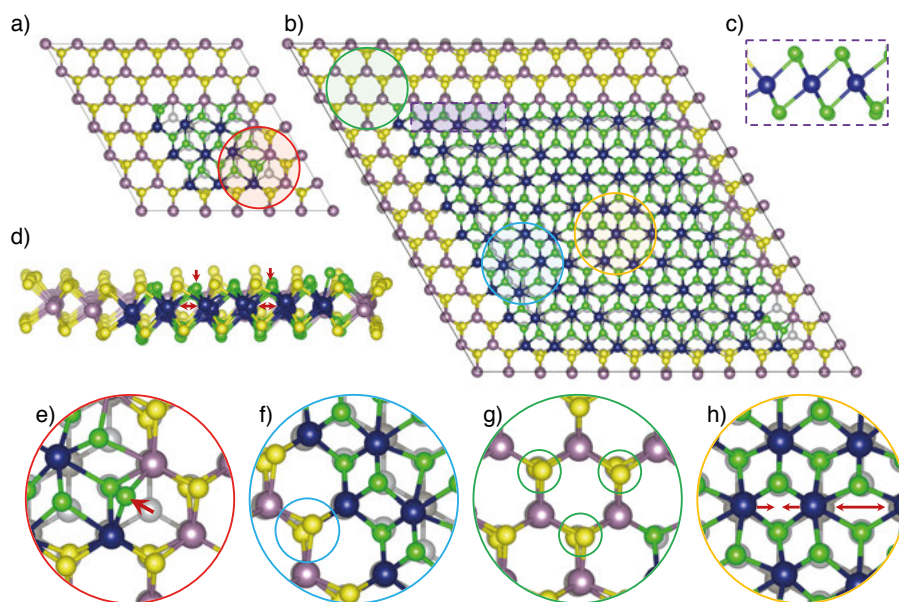
Figure 3.8. Structural reconstruction in the 1H-1T low energy composites (6-3 in (a) and 12-9 in (b)). Overlapping atomic positions before (grey) and after relaxation (following the color coding described in figure 3.6). c) Side view of the dashed purple rectangle in (b). d) Side view of the 1H-1T 9-6 in which the arrows point at the Mo-Mo dimerization features. (e-h) Zoomed regions enclosed by colored circles in (a) and (b). The arrow in (e) highlights a large atomic displacement, and the arrows in (h) show the direction of the Mo relaxation towards its dimerized positions. Reproduced with permission from Paper II.
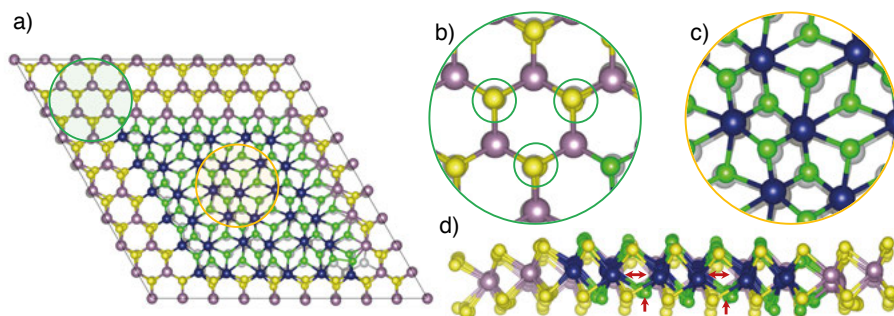

Figure 3.9. Structural reconstruction in the 1H-1T′ 6-3 composite. a) Overlapping atomic positions before (grey) and after relaxation (following the color coding described in figure 3.6). (b-c) Zoomed regions enclosed by colored circles in (a). d) Lateral view of (a) with arrows highlighting the features of Mo-Mo dimerization. Reproduced with permission from Paper II.

1T′. The 1H regions also suffer distortions: the S atoms in the 1H phase shift laterally in the 1H-1T composites (figure 3.8 (g)), but this is less evident in 1H-1T′. In general, smaller cells (6-3) are more distorted because they have a larger interface effect. However, the structural changes are also present in the center of the larger patches (12-9) as evident in figure 3.8 (h) and figure 3.9 (c), in which we see a clear tendency towards Mo-Mo dimerization after relaxation, which is characteristic for the 1T′ phase. We found that this was the reason why 1H-1T structures have larger reconstructions, since the cells starting with 1T′ were closer to the resulting positions. The dimerization of Mo atoms goes hand in hand with a vertical shift of the S atoms so that the S atoms in a long Mo-Mo bond come closer to the center of the layer and the ones in a short Mo-Mo bond go further away (see figure 3.8 (d) and figure 3.9 (d)). This tendency towards a 1T′-like phase in the patches of the mixed supercells can be explained by the relative stability of their pure phases, since 1T′ has a much lower energy than the unstable 1T.

In order to look for more evidence on the preference of 1T′, we plotted histograms for the nearest neighbor (NN) distances of Mo atoms (either S or Mo) in figure 3.10. If only pure phases were present, the histogram would have counts only at the characteristic NN distances of each pure phases. However, we observed that this was not the case, and that a dome around the 2.73 Å of the Mo-Mo short bond is present in all the cases. This means that even the supercells that had a starting 1T patch rearrange themselves favouring this dimerization. Given that the pure strained 1T′ phase is a small gap semiconductor, the tendency of the mixed structures to open a gap after relaxation can be explained.

3.2.4 Conclusions of Paper II

In this project we studied the effect of the coexistence of different polymorphs of MoS_2 using density functional theory. We showed that the reconstruction, which is not limited to the interface between two phases, is essential to explain the gap opening of the resulting structures, and can not be explained solely by the behavior of pure phases. We found that the reorganization inside the octahedral patch results in a dimerization of the Mo-Mo bonds, which shows a tendency towards a 1T′ structure. In this way, we explained that the small gap observed in some experiments is due to the interaction between different phases, rather than to a new pure metastable phase of MoS_2.
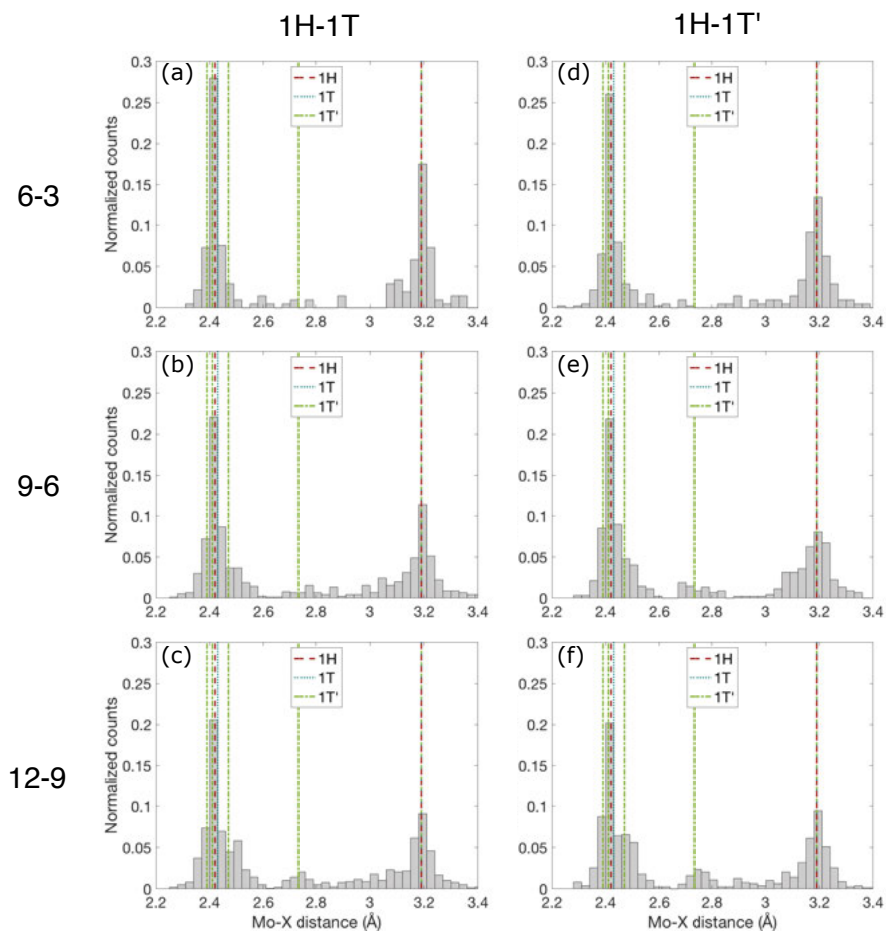
Figure 3.10. Probability normalized histograms of the Mo-X distance, X being a Mo nearest neighbor atom (Mo or S). (a-c) 6-3, 9-6 and 12-9 1H-1T, respectively. (d-f) 6-3, 9-6 and 12-9 1H-1T′, respectively. The vertical lines denote the pure phases nearest neighbor distances (red dashed for 1H, blue dotted for 1T and green dash-dotted line for 1T′).

4. RT-TDDFT studies of graphene flakes

La duda es uno de los nombres de la inteligencia.
(Doubt is one of intelligence's names)

Jorge Luis Borges

This chapter summarizes the results of Papers III and IV. Graphene has been studied since its experimental realization in 2004 [2] and it has shown to have many interesting properties [77–80]. However, it is a semimetal and therefore it is not a good candidate for transistor-based technology. One of the proposed ways to open up a gap in graphene to achieve a large on-off ratio is realizing nanostructures such as nanoflakes [81, 82]. In Papers III and IV we explored the optical properties of graphene nanoflakes using RT-TDDFT. In the first one, we focused on how the magnetic coupling of the edges and the corresponding optical properties can be tailored by the size and shape of the flakes, and in the second one, we explored their high harmonic response.

4.1 Summary of Paper III. Shape and size dependent optical spectra in magnetic GNF

In graphene nanoribbons, zigzag edges are antiferromagnetically coupled and armchair edges are non-magnetic [83], as figure 4.1 (a) and (b) depict. In Paper III, we focus on rectangular graphene nanoflakes (RGNF) because both zigzag and armchair edges are simultaneously present, raising the possibility of controlling the magnetic ground state of the nanostructure by modifying its size and shape. We denote RGNF following the convention used for nanoribbons [4, 83]: we classify them by the number of horizontal zigzag chains N_z and vertical armchair dimer lines N_a, and they are identified by $N_a \times N_z$-RGNF (see Figure 4.1).

4.1.1 Magnetism influences the optical spectra

In this paper, we considered two different magnetic alignments of the parallel zigzag edges: ferromagnetic (FM) and antiferromagnetic (AFM), as shown in figure 4.2 (b) and (c). We then calculated the optical absorption spectra of each
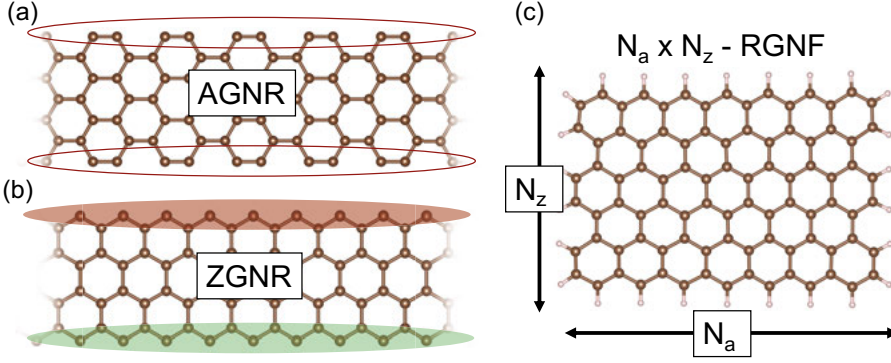
Figure 4.1. (a) Armchair graphene nanoribbon, the circles signal the parallel armchair edges being non-magnetic. (b) Zigzag graphene nanoribbon, the red and green circles show the parallel edges having opposite magnetic moment in an antiferromagnetic fashion. (c) Naming of the proposed rectangular graphene nanoribbons in terms of the number of armchair dimers N_a and zigzag chains N_z.
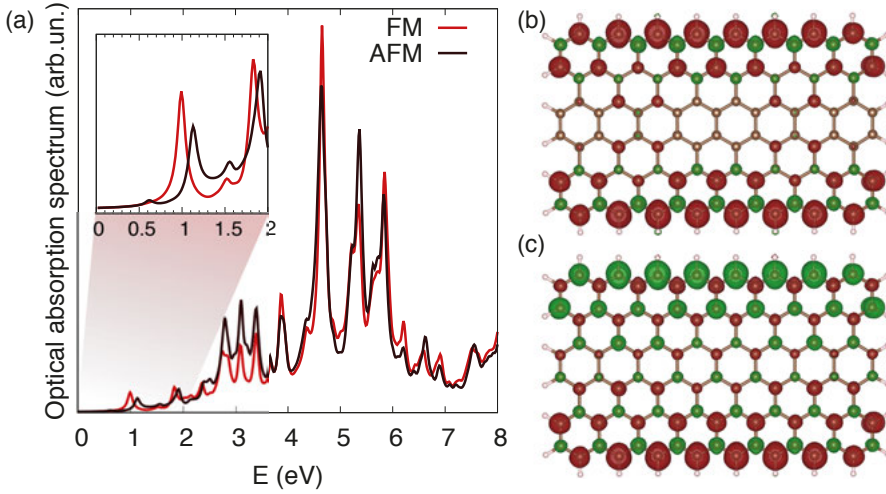
Figure 4.2. (a) Optical absorption spectra and magnetization densities for (b) ferromagnetically and (c) antiferromagnetically coupled edges in the 17×6-RGNF. The red (green) color represents positive (negative) magnetization density with an isovalue of $0.002 \ \mu_B/\text{Å}^3$. In the inset of (a), an expanded view of the optical absorption spectra at lower energies is shown. Reproduced with permission from Paper III.

flake using the method described in section 2.2.1, which is plotted in panel (a) of the same figure. As it can be seen, the higher end of the spectrum looks very similar for both FM and AFM flakes, but there is a clear shift of about 0.2 eV in the lowest energy peak. This is very interesting, because it means that the opacity of the flake to light of that energy range is different depending on the magnetic alignment of its zigzag edges.

We compared the total energy of the structure after atomic relaxation with AFM and FM coupling of the edges for RGNF with dimensions 17xN_z, with $N_z \in \{2, 4, 6, 8\}$ with parallel zigzag edges in its longer dimension. With this, we systematically studied the conditions of stability for the magnetic ordering, as the armchair length remains constant while the distance between the zigzag edges varies. The results are collected in table 4.1, where we can see that the AFM state is more favourable than the FM, but that energy difference decreases when the distance between the zigzag edges increases.

Table 4.1. *Energy differences between AFM and FM ordering, $\Delta E = E_{AFM} - E_{FM}$ for four different ratios of zigzag to armchair. To facilitate comparison with both GNRs and different kind of flakes, both the total energy and the energy per zigzag edge atom is specified. Energy units are in meV. Reproduced with permission from Paper III.*

Size	ΔE	ΔE/Zigzag edge atom	ΔE/atom
17×2	-133.42	-16.678	-2.471
17×4	-80.11	-10.014	-0.871
17×6	-71.45	-8.931	-0.550
17×8	-16.71	-2.089	-0.099

To understand the energy differences, we assumed that the dynamics of the edge magnetism is well described by a Heisenberg model, which we found to be a very good approximation for the larger flakes. Then the total energy difference is, to first order, given by the exchange coupling

$$\Delta E = J_{\text{Ex}} = E_{AFM} - E_{FM}, \tag{4.1}$$

where the sign of J depends on the convention used in the spin Hamiltonian. In order to achieve a switching between the ground state AFM state and the FM state, an external magnetic field needs to provide a Zeeman energy which is larger than the energy difference between the two states. As it is already known for ZGNR, this energy decreases monotonically with the increasing distance between the zigzag edges [84]. However, RGNF have about half of the coupling strength compared to ZGNR of the same width, which makes them more suitable for applications because smaller magnetic fields are needed. We attribute this smaller coupling in RGNF to the competition between zigzag edges' preference to be AFM and armchair edges to be non-magnetic, together with the magnetic frustration that happens in the center of the flake for the AFM case and is not present in the FM case (see figure 4.2).

4.1.2 Shape and size dependence on the optical spectra

Changing the size and shape of the flakes can, besides tailoring the strength of the magnetic coupling, change the position and structure of the peaks present in the optical spectrum. Therefore, in this part of the paper we explored the

possibility of having different hexagonal shaped flakes as well as changing the size of the RGNF in a systematic way.

One might be tempted to think that zigzag edges are the ones responsible for the magnetism in GNF, but we constructed two hexagonal flakes with only zigzag edges (coronene and its larger analogue $C_{130}H_{28}$) and found them not to be magnetic, in line with what has been reported for hexagonal and triangular shapes in [85]. However, we can observe the size effects in their optical absorption spectra, which is shown in figure 4.3, together with their structure. In the total spectrum (a) we see that the the coronene peaks are present in $C_{130}H_{28}$, only shifted to lower energies due to quantum confinement, and that the large flake has multiple peaks at lower energies. Furthermore, the triple peak structure at around 6 eV in the x-direction is present in both systems as well.
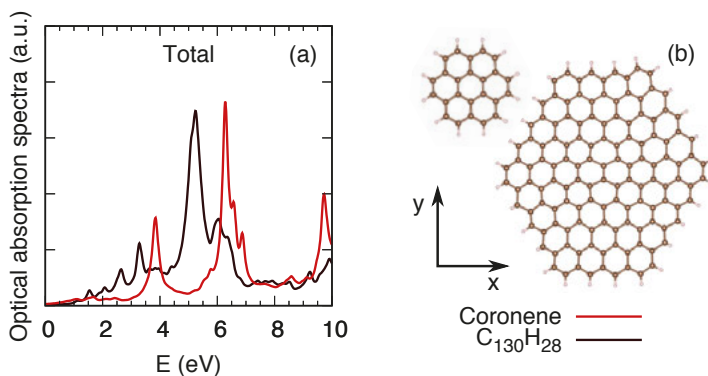

Figure 4.3. $C_{130}H_{28}$ and coronene normalized optical spectra. (a) shows the total optical absorption spectra, (b) shows the relaxed structures for both molecules, with carbon (hydrogen) atoms represented in brown (white).

To study the contribution of zigzag and armchair edges in RGNF in a systematic way and their effect on the optical spectra we built two series of RGNF, as shown in figure 4.4. The starting point is a 7×6-RGNF which we extend in the x and y direction separately: constant armchair flakes in (a) are constructed by increasing its size by two vertical dimer lines, while constant zigzag flakes grow by adding two horizontal zigzag lines. In figure 4.4 (c-d) we plot the directional dependence of the optical absorption spectra for each of the flakes, where we observe the expected trend in closing the gap for smaller sizes (due to quantum confinement and as it was shown for the hexagonal flakes). The green trend line is a guide for the eye that follows the position of the highest peak, and shows that with increasing flake size the main peak position shifts to lower energies only in the direction parallel to the applied electric field (see panels (c) and (f)), while applying an electric field parallel to the edge that is kept constant shows no peak shift (see panels (d) and(e)).
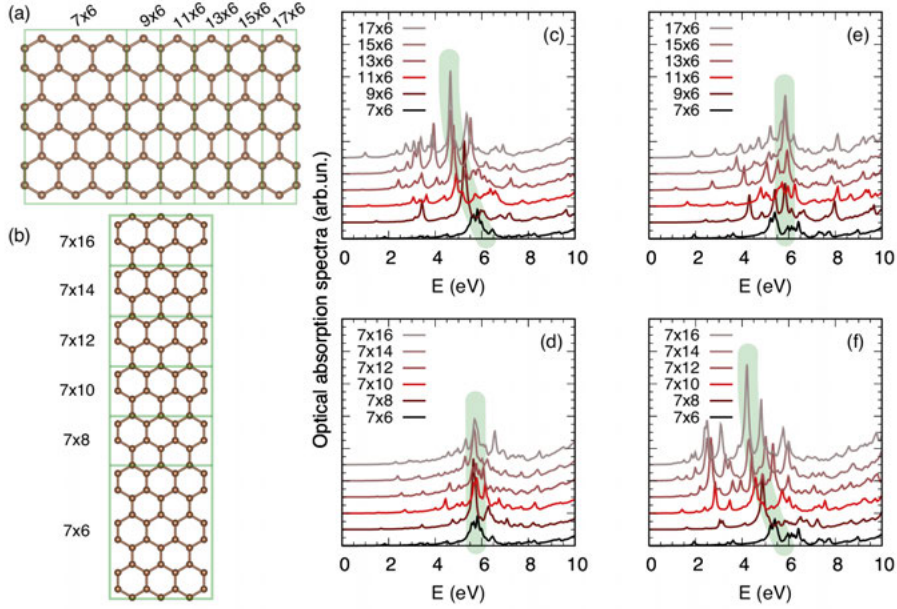
Figure 4.4. Size effect on the optical spectra of RGNF. Panel (a) shows the structures of the rectangular flakes with constant armchair edge and flakes with constant zigzag edge are shown in (b). In both (a) and (b), carbon atoms are represented in brown and the passivating hydrogens are not drawn for the sake of clarity. (c-f) contain the rectangular flakes' in-plane optical spectra for different sizes and electric field directions (x-direction is parallel to the zigzag edge and y-direction is parallel to the armchair edge), obtained from TDDFT calculations. Panel (c) shows the x-component of the optical spectra for the flakes with constant armchair edge, panel (e) shows the y-component for the same flakes. (d) contains the x-component for the constant zigzag-edged flakes and finally (f) shows their y-component.

4.1.3 Conclusions of Paper III

In this paper, we used RT-TDDFT to show that the magnetic exchange coupling between zigzag edges can be tailored by optimizing the size and shape in rectangular graphene nanoflakes. We observed as well that there is a possibility of altering the optical response of the flakes (their opacity) via switching between two magnetic states (AFM and FM coupling of the zigzag edges) using magnetic fields. Therefore, we have proposed a route to design energy-efficient optoelectronic devices by choosing the size and shape of the flakes to fit the desired purposes.

4.2 Summary of Paper IV: High harmonic generation

In Paper IV, we studied the HHG of a 17×6 rectangular graphene nanoflake that was introduced in Paper III using RT-TDDFT. We showed that the different electronic structure (and thus linear optical absorption spectrum) given by ferromagnetic and antiferromagnetic coupling of the zigzag edges has a clear effect on the harmonic yield.

4.2.1 Calculation of the HHG spectrum

As shown in (2.42) of section 2.2.1, we calculated the HHG spectrum from the dipole velocity, following the derivation in [42]:

$$\text{HHG}_{j,k}(\omega) \propto \text{FT}\left[\left|\dot{p}_{j,k}(t)\right|^2\right]. \tag{4.2}$$

Several publications [39–41] follow the acceleration theorem and therefore obtain:

$$\text{HHG}_{j,k}^{acc}(\omega) \propto \frac{1}{\omega^2}\text{FT}\left[\left|\ddot{p}_{j,k}(t)\right|^2\right]. \tag{4.3}$$

If the dipole was used directly, the equation would read:

$$\text{HHG}_{j,k}^{dip}(\omega) \propto \omega^2\text{FT}\left[\left|\dot{p}_{j,k}(t)\right|^2\right]. \tag{4.4}$$

We compared the spectra resulting from these 3 equations and found that the position of the peaks is the same, and that the low order curves are quite similar. However, the dependence on ω induces a slope on the curve, which is visible at high order but also in the depth of the valleys between peaks already at low order. This is shown in figure 4.5 and is consistent with what was reported in [42].
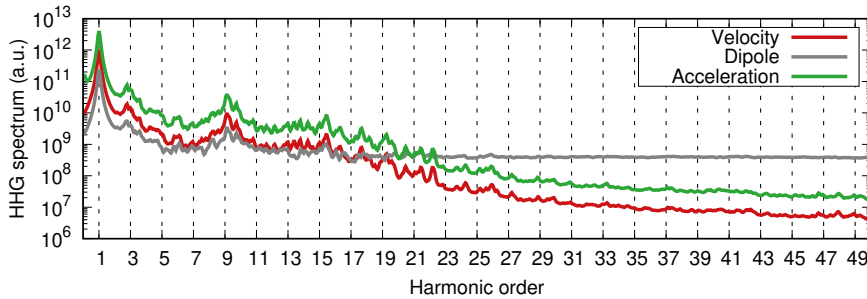

Figure 4.5. HHG for a RGNG with FM coupling of the zigzag edges. Comparison of the spectrum resulting from the velocity of the dipole in red (see equation (4.2)), the dipole in grey (see equation (4.4)) and its acceleration in green (see equation (4.3)).
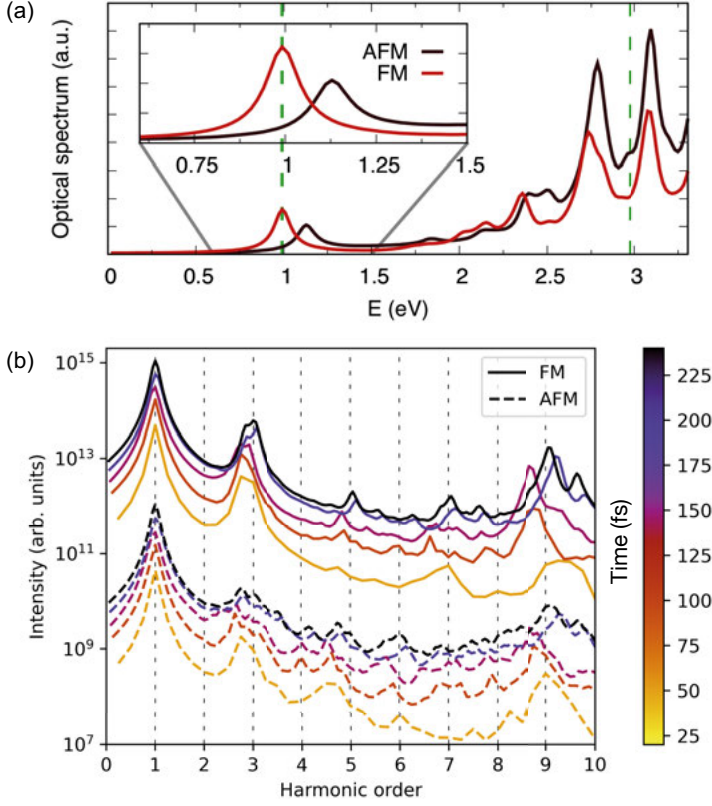
Figure 4.6. (a) Optical absorption spectra for both magnetic configurations. The inset shows an expanded view of the first peak. The green dashed lines mark the energies of the 3rd and 9th harmonics corresponding to the HHG spectrum in (b). (b) Harmonic yield as a function of time, where time represents the duration of a rectangular envelope.

4.2.2 Harmonic yield dependency on the pulse duration and the presence of resonances

In order to investigate the contribution of the bound states beyond the ground state to the HHG we studied the case where the third harmonic coincides with a peak in the linear absorption spectrum. We fixed the pump frequency to be 1/3 of the first peak in the FM linear absorption, which is not a resonance in the linear spectrum for the AFM flake (see figure 4.6 (a)). This pump frequency is below the optical gap and therefore no linear processes are present, so it is a good tool to evaluate how the excited bound states affect higher order processes. With the help of a wavelet-transform analysis, we studied the harmonic yield for different pulse duration and the results are shown in figure 4.6 (b). Focusing on the third harmonic peak, which is allowed by symmetry, we observed that for short pulses the yield is very similar for both AFM and FM

flakes, but that it is suppressed for long pulses in the AFM case. The intensity is approximately 5 times higher in the FM flake at 240 fs pump duration. It is interesting to see that the 9th harmonic yield is similar for both magnetic configurations, and this is given by the fact that it falls very close to a resonance at 3 eV which is not significantly shifted.

We then explained this behaviour with a model of superposition of coupled oscillators. We can assume that the linear absorption spectrum is a sum of direct dipole transitions, and that they interact through the electromagnetic field. The superposition of the linear resonance and the third harmonic can produce beatings and have a phase mismatch, which depends on the damping and the frequency matching. This analysis confirms that the 3rd harmonic yield is quenched in the AFM coupling due to destructive interference, which becomes more apparent for long pump pulses.

4.2.3 Conclusions of Paper IV

In Paper IV we used RT-TDDFT to study high harmonic generation, a non-linear phenomena, in the rectangular graphene nanoflakes that were introduced in Paper III. We showed that different magnetic configurations (ferro- and antiferromagnetic coupling of the zigzag edges) have an effect on the high harmonic generation. This can be explained by the interference of the harmonic field and the fundamental one, depending on the distinct underlying electronic structure.

5. Diffuse scattering in SnSe

*One never notices what has been
done; one can only see what
remains to be done.*

Marie Skłodowska Curie

5.1 Summary of Paper V

In paper V, we combined ultrafast photoinduced diffuse scattering (PSD) with
rate equations simulations following the methodology described in section
2.3. We studied the non-equilibrium energy transfer between electrons and
phonons after a photoexcitation in order to understand the thermalization dynamics of SnSe.

5.1.1 *Ab initio* simulations

We calculated the phonon band structure and phonon-phonon scattering matrices for bulk SnSe from *ab initio* methods. The crystal structure of SnSe
and its high symmetry points in the Brillouin zone are shown in figure 5.1.
Its phonon band structure along a high symmetry path and phonon density of
states, which agree with previously reported studies [86], are shown in figure
5.2.

The figure of merit zT for a thermoelectric material is a measure of how
high the thermoelectric conversion energy is. It is defined as

$$zT = \frac{S^2 \sigma T}{\kappa},\qquad(5.1)$$

where S is the Seebeck coefficient, σ is the electrical conductivity, T is the
temperature and κ is the thermal conductivity (sum of electronic and lattice
contributions). Therefore, a material with a high figure of merit needs to have
a low lattice thermal conductivity and high electrical conductivity. SnSe has
been proposed as a good thermoelectric material due to its remarkably low κ
[7]. From our simulations, we obtained lattice thermal conductivities of 1.669,
0.987 and 0.683 W/mK at 300K, for the a, b and c directions respectively,
which agrees quite well with the experimental results. Since phonons are the
main energy carriers in SnSe, we studied the phonon scattering dynamics in
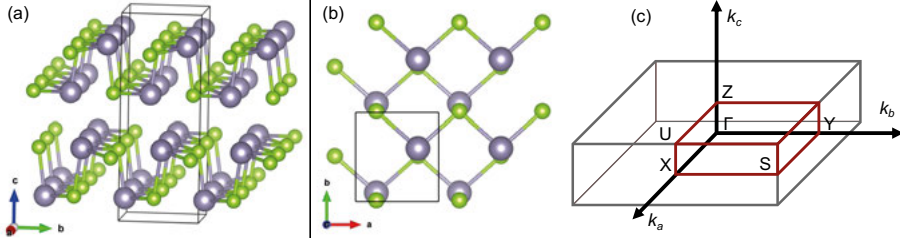order to better understand the thermal properties of this material.

Figure 5.1. (a-b) Crystal structure of bulk SnSe. Se atoms are green and Sn atoms are grey. The black lines show a unit cell. (c) First Brillouin zone and high symmetry points of the *Pnma* space group, to which bulk SnSe belongs.
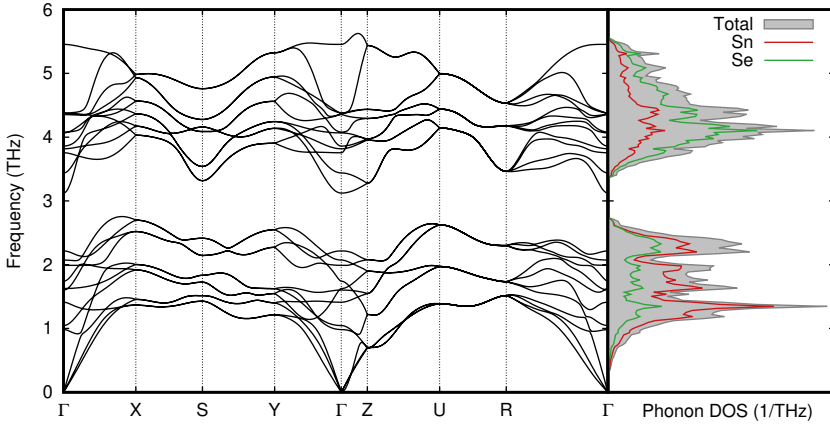

Figure 5.2. Left: Phonon spectrum of SnSe along high-symmetry points in the Brillouin zone. Right: total phonon density of states in shaded grey, and projection to the Sn and Se atoms in red and green lines, respectively.

5.1.2 Rate equations simulations

The *ab initio* phonon frequencies and phonon-phonon scattering matrix elements have been used as input for the nonequilibrium kinetic simulations that describe the energy flux between the electronic and phononic systems as described in section 2.3. Our collaborators in KTH performed time-resolved ultrafast electron diffraction experiments in order to obtain the photoinduced diffuse scattering dynamics of SnSe samples. As mentioned in section 2.3.2 diffuse scattering occurs due to non-elastic scattering events mediated by the lattice vibrations, and studying its time dependence provides information on phonon dynamics. The comparison of the theoretical and experimental results is given in figure 5.3. Here, the electron-phonon coupling was taken as a fitting parameter to the experimental data, and more details about that are given in the supplementary information of Paper V. In the future, the q-dependent

electron-phonon coupling will be calculated from ab initio theory to have a more profound comparison with experiment.

The complex dynamics observed for four different q points in the reciprocal space can be explained by the competition between different energy transfer channels, and an increase or decrease of intensity is related to an imbalance between the incoming and outgoing energies at that q point. The experimental and theoretical data are in good agreement regarding the general dynamics as evident in figure 5.3. From our simulations, we found that the three acoustic branches and the lowest three optical branches are the ones that contribute most to the dynamics. The photoinduced diffuse scattering intensity of each phonon mode is proportional to its energy and population, which means that that the higher energy phonons are populated faster than the low-lying ones. Therefore, increase of intensity seen in figure 5.3 for all the four cases after photoexcitation is due to the energy flow from the electrons to the high energy phonon branches. After this high electron-phonon transfer in the early time scale, the energy redistributes via phonon-phonon scattering channels among different phonon modes, first with a decrease followed by an increase in a non-trivial manner.

5.2 Conclusions of Paper V

In Paper V we used rate equations to study the phonon dynamics in SnSe, a good thermoelectric material. We showed that the non-trivial dynamics at selected points in the reciprocal space can be explained by a complex energy transfer between the electronic and phononic systems. Our results agree reasonably well with the time-dependent diffuse scattering experiments.
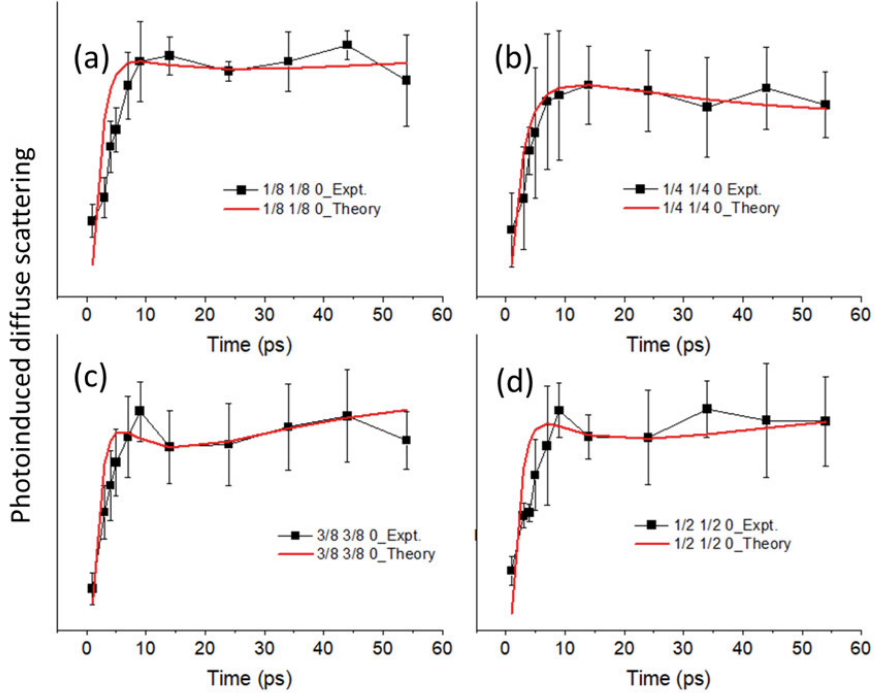
Figure 5.3. Temporal evolution of photoinduced diffuse scattering in SnSe for four different q points. These points are (a) $q = (1/8, 1/8, 0)$, 12.5% along $\Gamma_{[020]} - X + \Gamma_{[011]}$, (b) $q = (1/4, 1/4, 0)$, 25% along $\Gamma_{[020]} - X - \Gamma_{[011]}$, (c) $q = (3/8, 3/8, 0)$, 37.5% along $\Gamma_{[020]} - X + \Gamma_{[011]}$ and (d) $q = (1/2, 1/2, 0)$, 50% along $\Gamma_{[020]} - X + \Gamma_{[011]}$ (the positions of the Bragg peaks given by [xyz] correspond to figure 2 in Paper V). Black points are experimental data and the red line is the theoretical model. Figure produced by Amit Kumar Prasad.

6. Conclusions and Perspectives

For even the very wise cannot see all ends.

Gandalf the Grey

This thesis is an overview of some of the theoretical methods available to study electronic excited state dynamics in extended systems, and how to walk from the full quantum treatment to the different flavours of Mixed Quantum-Classical methods, which are based on Density Functional Theory. With those at hand, I have tried to answer, together with my collaborators, several questions about time-dependent processes in two-dimensional systems like MoS_2, graphene flakes and bulk SnSe. The detailed conclusions we reached in each project can be found in their respective chapters and papers, but I would like to discuss what could come next. What can be done to continue the investigations in those systems? Can we do better? I believe there is always room for improvement and I will try to address this in the next paragraphs.

In Paper I, we could look into the back-reaction of the electronic dynamics onto the ionic motion if we did not work with precomputed ionic trajectories. We could even wish to go beyond the one-particle picture to be able to include excitonic effects, which can be important in MoS_2. However, both ideas are far from being computationally feasible for the systems' size and length scales of the dynamics we studied. Instead, I would tackle the problem using the recent developments that correct the phase of the wave function at each time step in order to get more correct non-adiabatic coupling matrix elements for obtaining more accurate dynamics. In Paper II, we tried to understand the behaviour of samples that mix different phases of MoS_2. We could look into more interface structures between the phases and explicitly study the possible atomic diffusion at the boundaries using Molecular Dynamics or the Nudged Elastic Band method to have access to the diffusion energy barriers.

Paper III investigates the coupling between magnetic and optical properties in graphene nanoflakes. Of course, RT-TDDFT is not necessary to calculate optical spectra, as linear response methods are often enough. Nevertheless, those would allow for the use of better time-dependent exchange correlation potentials beyond the adiabatic one we used. However, this project opened the door to Paper IV, in which we study high harmonic generation (HHG) in the same systems. Being a higher order process, HHG could not have been observed using the methods that could have improved the first paper. A continuation of Paper IV would be trying to better understand our observations,

possibly in a simpler system for which we could analyze the phase of the wavefunction in a systematic way.

Finally, in Paper V, we used rate equations to understand the experimental results of diffuse scattering in SnSe. As a first improvement, electron-phonon coupling could be extracted from *ab initio* calculations, just as we did with phonon-phonon scattering matrix elements. At a higher level, the theory could be improved by considering that the electron system also consists of subsystems that interact with each other, so that the energy flow would be between electron-electron, phonon-phonon and electron-phonon systems.

As it can be seen, this is an *exciting* field with many paths to explore!
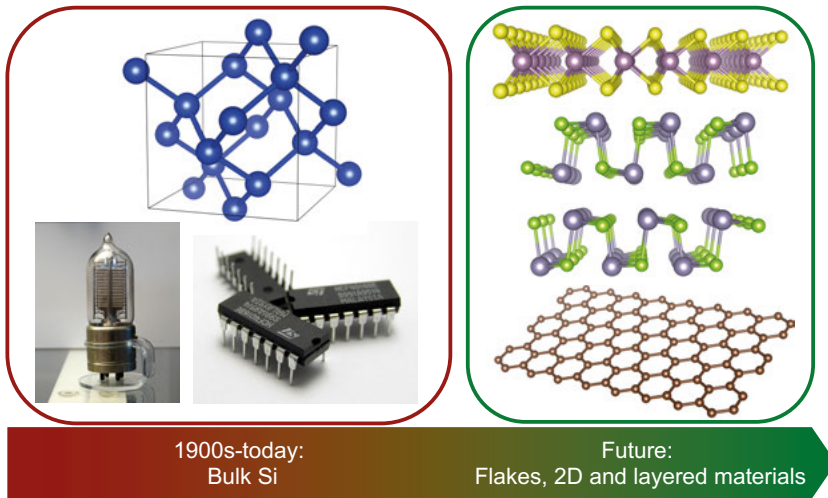
Popular science summary

Figure 6.1. Evolution of the electronic materials from bulk Si to the future suggestions discussed in this thesis. In the red panel: bulk Si crystal structure, a vacuum tube from the beginning of electronics, and modern integrated chips. In the green panel, from top to bottom: monolayer MoS_2, layered SnSe and a rectangular graphene flake.

We have been using tools even since before we became humans. Choosing natural materials and modifying them to suit our needs is a part of the development of our species, and tools have been evolving accordingly from stone knives to plastic bottles and mobile phones. We are surrounded by electronics: from the simplest digital watch to the Perseverance Rover from NASA that is exploring Mars, our world depends on efficient electronic devices. They are based on a class of materials called semiconductors, which allow turning them "on" and "off". For more than a century, bulk silicon has been the go-to semiconductor because it is cheap and has the right properties. As technology advanced, electronic devices have become smaller with time. However, their miniaturization can not continue forever because when three dimensional materials reach a small enough size, heating and quantum effects become problematic. One of the routes towards smaller scales is to build devices made

from two-dimensional materials, because their thickness is the smallest we can think of, just one or few atoms. The most famous of these monolayer materials is graphene, a single layer of graphite, which is what the inside of pencils are made of. Its discovery was a revolution because it opened the door to study two-dimensional materials. However, graphene is not a semiconductor, because it is very difficult to distinguish between its "on" and "off" states, which limits its use as a silicon substitute. This can be improved in different ways, and a large part of this thesis focuses on alternative two-dimensional materials to graphene that are semiconductors. One way is to cut pieces of graphene in the shape of flakes, and another one is to go to other materials that can also be made two-dimensional. One of them is monolayer MoS_2 (molybdenum disulfide) which is a good semiconductor. Besides being promising candidates to substitute silicon in electronics, 2D materials and bulk materials that are made from layers have been investigated with other applications in mind, one of which is the exploitation of their capability to convert thermal into electrical energy. Thermoelectric materials such as SnSe (tin selenide) lead a way into environmentally friendly power generation processes, and therefore studying their fundamental properties at the atomic scale is crucial for the development of this field.

Most of nature's phenomena are processes that are far from equilibrium, they are changes from one state to another. The question of how to study such processes is still open, because it is a very complex one. With the development of state-of-the-art experimental techniques, nowadays it is possible to study many physical phenomena in an atomistic and electronic scale, even the dynamics in an ultrafast time scale. However, the experimental observations need advanced theoretical and computational methods to analyze the data in order to have a proper understanding. In this thesis, we dig into this field and try to study out-of equilibrium processes from a theoretical point of view. There are relatively accurate solutions to these kind of problems for very small systems such as atoms and small molecules but extended systems such as 2D materials and bulk solids still remain a challenge. Atoms are formed by their nucleus, which we could consider to be ions, and electrons, and both follow the laws of quantum mechanics. However, solving the necessary quantum-mechanical equations for both electrons and ions is an impossible task. Many approximations need to be made, and the most important one is the neglect of the quantum nature of the ions composing the material. These groups of methods, in which ions are treated classically and electrons quantum-mechanically, are called semiclassical methods and they are the basis of what is discussed in this thesis. We use them in order to understand non-equilibrium processes in the materials that have been discussed in the previous paragraph, in order to progress in the quest towards smaller and more efficient electronic devices.

Populärvetenskaplig samanfattning
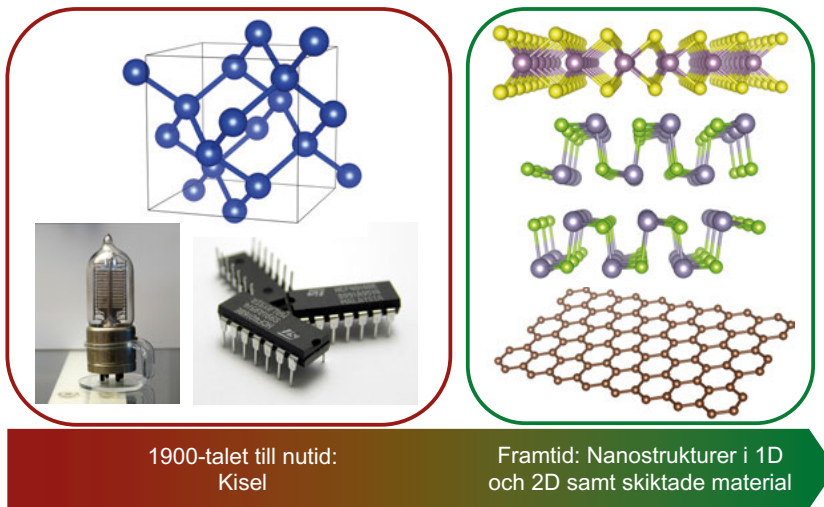
Figur 6.2. Illustration av utvecklingen av elektroniska material från bulk-Si till framtida förslag som diskuteras i denna avhandling. I den röda rutan: bulk-Si-kristallstruktur, ett vakuumrör och moderna integrerade chip. I den gröna rutan (uppifrån och ner): monolager MoS_2, skiktad SnSe och en rektangulär grafenflinga.

Vi tillverkade och använde verktyg redan innan vi blev moderna människor. Att välja naturmaterial och modifiera dem för att passa våra behov är en del av utvecklingen av vårt art, och verktyg har utvecklats därefter från stenknivar till plastflaskor och mobiltelefoner. Idag är vi omgivna av elektronik: från den enklaste digitala klockan till Perseverance Rover från NASA som utforskar Mars, vår värld är beroende av effektiva elektroniska enheter. De är baserade på en klass av material som kallas halvledare, vilket gör det möjligt att slå på och stänga av dem. I mer än ett sekel har bulk kisel (Si) varit den mest använda halvledaren eftersom det är billigt och har rätt egenskaper. I takt med teknikens framsteg har elektroniska enheter blivit mindre, men dess miniatyrisering kan inte fortsätta för alltid, för när tredimensionella material når tillräckligt liten storlek blir värme- och kvanteffekter problematiska. Ett alternativ för att möjliggöra ännu mindre enheter är att tillverka dem av tvådimensionella material, eftersom deras tjocklek är den minsta vi kan tänka oss, bara en eller några få atomer. Det mest kända av dessa enskiktsmaterial är grafen, som består av ett enda lager grafit, vilket är vad insidan av pennor är gjorda av. Upptäckten var

66

en revolution eftersom den öppnade dörren för att studera tvådimensionella material. Grafen är emellertid inte en halvledare, eftersom det är mycket svårt att skilja mellan dess "på" och "av" -tillstånd, vilket begränsar dess användning som ersättningsmaterial för kisel. Detta kan dock förbättras på olika sätt, och en stor del av denna avhandling fokuserar på alternativa tvådimensionella material till grafen som är halvledare. Ett sätt är att skära bitar av grafen i form av flingor, och ett annat är att vända sig till andra material som också kan göras tvådimensionella. Ett av dem är monolager MoS_2 (molybdendisulfid) vilket är en bra halvledare. Förutom att vara lovande kandidater för att ersätta kisel i elektronik har både 2D- och bulkmaterial som tillverkats av lager undersökts med andra applikationer i åtanke, varav en är utnyttjandet av deras förmåga att omvandla termisk till elektrisk energi. Termoelektriska material, som SnSe (tinselenid), leder en väg mot miljövänliga kraftgenereringsprocesser, och därför är det viktigt att studera deras grundläggande egenskaper på atomnivå för utvecklingen av detta fält.

De flesta av naturens fenomen är processer som befinner sig långt ifrån jämvikt, de innebär förändringar från ett tillstånd till ett annat. Frågan om hur man studerar sådana processer är fortfarande öppen, eftersom den är mycket komplex. Med utvecklingen av toppmoderna experimentella metoder är det numera möjligt att studera många fysikaliska fenomen på atomära och elektroniska längdskalor, inklusive dynamiska tidsförlopp. De experimentella observationerna behöver dock avancerad teori samt beräkningsmetoder för att analysera data och på så sätt få en korrekt förståelse för det studerade förloppet. I denna avhandling fokuserar vi på detta ämnesområdet och försöker studera processer utanför jämvikten ur en teoretisk synvinkel. Det finns relativt noggranna lösningar på denna typ av problem för mycket små system såsom atomer och små molekyler, men utökade system som 2D- och bulkmaterial är fortfarande en utmaning. Atomer består av deras kärna, som vi kan betrakta som joner, och elektroner, och båda följer kvantmekanikens lagar. Att lösa de nödvändiga kvantmekaniska ekvationerna för både elektroner och joner är dock en omöjlig uppgift. Många approximationer måste göras, och den viktigaste är försummelsen av jonernas kvantegenskaper. Dessa grupper av metoder, där joner behandlas klassiskt och elektroner kvantmekaniskt, kallas semiklassiska metoder och de är grunden för vad som diskuteras i denna avhandling. Vi använder dem för att förstå icke-jämviktsprocesser i materialen som har diskuterats i föregående stycke, för att gå vidare i strävan efter mindre och mer effektiva elektroniska enheter.
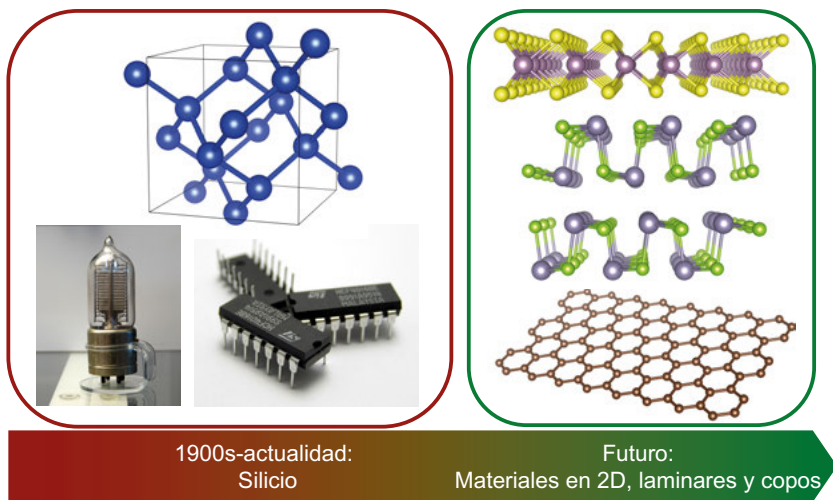
Resumen divulgativo

Figura 6.3. Evolución de los materiales usados en electrónica desde el silicio hasta los materiales del futuro que se proponen en esta tesis. En el recuadro rojo: estructura cristalográfica del silicio en 3D, válvula de vacío usada en los inicios de la electrónica y chip integrado moderno. En el recuadro verde, de arriba a abajo: MoS_2 monocapa, SnSe en capas, copo rectangular de grafeno.

Hemos usado herramientas desde antes de convertirnos en humanos. Escoger materiales que nos ofrece la naturaleza y modificarlos para cubrir nuestras necesidades es parte del desarrollo de nuestra especie, y las herramientas han ido evolucionando desde cuchillos de piedra de la prehistoria hasta las botellas de plástico y los teléfonos móbiles de hoy en día. Estamos rodeados de electrónica: desde el reloj digital más simple al robot Perseverance de la NASA que está explorando Marte, nuestro mundo depende de aparatos electrónicos eficientes. Están basados en una clase de materiales llamados semiconductores, que permiten que puedan estar apagados y encendidos. Durante más de un siglo, el silicio ha sido el semiconductor más común porque es barato y tiene las propiedades adecuadas. A medida que la tecnología ha ido avanzando, el tamaño de los aparatos electrónicos se ha ido reduciendo. Sin embargo, su miniaturización no puede continuar para siempre porque cuando materiales en tres dimensiones se vuelven lo sufiencientemente pequeños, se calientan demasiado y aparecen otros efectos de origen cuántico que son problemáticos. Uno de los caminos para conseguir reducir el tamaño pasa por fabricar

aparatos con materiales bidimensionales ya que tienen el grosor más pequeño que podemos imaginar: tan solo uno o pocos átomos. El grafeno es el más conocido entre ellos, y está compuesto por una sola capa atómica de grafito, el material de las minas de los lápices. Su descubrimiento fue una revolución porque abrió la puerta a un nuevo campo de investigación. No obstante, el grafeno no es un semiconductor, lo que hace que sea muy difícil distinguir entre sus estados de apagado y encendido, así que no es un buen candidato para substituir al silicio. Esto se puede mejorar de diferentes maneras, y una gran parte de esta tesis está centrada en materiales bidimensionales alternativos al grafeno que sí son semiconductores. Una opción es cortar trozos de grafeno en lo que se llaman copos, y otra es considerar otros materiales que también son bidimensionales. Uno de ellos es MoS_2 (disulfuro de molibdeno) bidimensional. A parte de ser buenos candidatos para substituir al silicio en la electrónica, tanto materiales bidimensionales como otros en tres dimensiones pero que están formados por capas atómicas se han investigado con otras aplicaciones en mente. Una de ellas es aprovechar la capacidad que tienen algunos para convertir energía térmica en eléctrica. Materiales termoeléctricos como el SnSe (seleniuro de estaño) abren el camino a procesos de generación de energía que sean respetuosos con el medio ambiente, y es por eso que estudiar sus propiedades fundamentales a nivel atómico es crucial para el desarrollo de este campo.

La mayoría de los fenómenos naturales están lejos del equilibrio y son cambios de un estado a otro. La cuestión de cómo estudiar este tipo de procesos es muy compleja y está aún abierta. Con el desarrollo de técnicas experimentales punteras es posible estudiar muchos fenómenos físicos a nivel atómico y electrónico, incluso su dinámica ultrarrápida. Sin embargo, se necesitan métodos teóricos y computacionales para analizar los datos experimentales y entenderlos debidamente. En esta tesis nos adentramos en este campo e intentamos estudiar procesos fuera del equilibrio desde un punto de vista teórico. Existen soluciones relativamente precisas para sistemas muy pequeños como átomos y moléculas pequeñas, pero son todavía un desafío para otros más extensos como materiales bidimensionales o sólidos tridimensionales. Los átomos están formados por su núcleo, también llamado ión, y electrones, y ambos se comportan según las leyes de la mecánica cuántica. Sin embargo, resolver las ecuaciones cuánticas necesarias para iones y electrones es imposible. Son necesarias muchas aproximaciones y la más importante es omitir la naturaleza cuántica de los iones. Este grupo de métodos en los que los iones se tratan de forma clásica y los electrones de manera cuántica, se llaman métodos semiclásicos y son la base de lo que se describe en esta tesis. Los usamos para entender procesos fuera del equilibrio en los materiales que se han mencionado en el párrafo anterior, con el objetivo de progresar en la búsqueda de aparatos electrónicos más pequeños y eficientes.

Acknowledgements

That was fun. Let's never do that again.

Chris Pontius

First of all, I would like to thank my supervisors because this thesis would not have been possible without them. Thank you Biplab for being so enthusiastic and always full with ideas for new projects. Thank you for believing in me after my master thesis and giving me the chance to continue here. Thanks to Oscar for jumping aboard with your optimism and time-dependent knowledge, you were always ready to discuss (seriously or over coffee) and that was extremely useful. I would also like to thank Susanne for being part of the team for a short while, but being always available after that as well.

In my PhD I participated in very interesting collaborations that were possible thanks to the work of my coauthors: Pujari, DD Sarma, Alexey, Amit, Jonas and Pablo. Thank you for your work and for great discussions. During my time here I enjoyed being part of Biplab's research group because I had the chance to meet great people. Thanks to Carmine and Soum for helping me settle in when I started, to Xin and Duo for fun breaks and discussions, to Suhas for being a great half-member of the group, and to our temps Bo and Bruno for good times while they were here.

Shout-out to my office mates, past and present, for making this the best office. Iulia and Jakob, you made sure that I had enough daily chocolate and crazy conversation topics. I really hope there was no listening device in the room! Uli, you were probably not the best for my productivity (same as I wasn't for yours) because we could talk for hours! Thanks for introducing me to great music for every mood (watermelon song!) and showing me how cool penguins are. Alena, thanks for the all-holiday office decoration, the coffee machine and for trying to transform me into a more adventurous person. I am sorry you failed miserably as much as I tried to improve your food taste (Rafael, we tried hard), total lost cause! Thanks to Simon for putting up with us two, even if the pandemic made it a quite short time.

I still remember the coffee walks, lunches and fikas from pre-covid times. Thanks to everyone that made those breaks enjoyable: Alex, Rafael, Leandro, Heike, Erna, Barbara, Yaroslav, Renan, Vlad... and everyone else in the division that contributed to a friendly atmosphere.

After some years in Uppsala, I have met some people that make life more fun and easy. Gràcies Jordi-Lluís, Joana and the kids Gerard and Linnéa for

70

fun "picnics" and always being ready to help. Also gracias Pablo, Ana and the kids Pablo and Mateo for barbecues and other outings. To Nikos, Katerina, Agnė and Oscar for exploring nations together and having so many potluck dinners. Fun times! Thanks to Elin for being around for so long, and specially now for our coronaanpassade walks. They keep me sane!

My very critical proof-reading committee was formed by Fabian, Duo and Adri. Sorry that you had to read everything so careful, your comments were priceless! Special thanks to Fabian for being such a big support and inspiration in many aspects, you're awesome. Also to Duo for being so fun and positive. Sports with you two guys was one of the best things of these last years, thanks for that!

I would not be here if I hadn't passed my bachelor courses, and a quite large group of people from the Uni in Barcelona has a lot to do with that. Gràcies Físics! You made those years so much easier with your jokes, crazy parties, beers, late nights and also long studying hours in the library. Thanks to you I learned the importance of power naps, selectas and tupperwares filled with tasty food. And maybe some physics too.

Thanks to Mireia and Maria for making me laugh until my cheeks hurt, you rock! Noe, I still keep your phone contact as "Noe electronica" but what started in those lectures has brought us so far! Thanks for our long talks, laughs and being ready to help. Thanks to my cousin Marta for being a role model and such an awesome person to be around.

I should mention my family for being so supportive and caring: Amelia, José Ramón, Irene, Pablo, Yaya Meli, Yayo Luciano, and also the ones that will read this from somewhere else: Yaya Encarna and Yayo Andrés. Of course, very very special thanks to my parents Andrés and Conchita, I would not be here without your help, support and everything you taught me. The coolest brother on earth (Víctor) deserves a big thanks for everything, but specially for the great bad jokes. Also Maui for cuddles, drool and making every day a surprise.

And last but not the least thanks to Adri, the best partner I could ever ask for. You take care of me and make me become the best version of myself, and I am looking forward to see what this next step in life will bring us.

References

[1] P. R. Wallace, "The band theory of graphite," *Physical Review*, vol. 71, pp. 622–634, may 1947.

[2] A. Novoselov, K.S., Geim, A.K., Morozov, S.V., Jiang, D.A., Zhang, Y., Dubonos, S.V., Grigorieva, I.V. and Firsov, "Electric field effect in atomically thin carbon films," *Science*, vol. 306, no. 5696, pp. 666–669, 2004.

[3] R. Martinazzo, S. Casolo, and G. F. Tantardini, "Symmetry-induced band-gap opening in graphene superlattices," *Physical Review B*, vol. 81, p. 245420, jun 2010.

[4] M. Fujita, K. Wakabayashi, K. Nakada, and K. Kusakabe, "Peculiar Localized State at Zigzag Graphite Edge," *Journal of the Physical Society of Japan*, vol. 65, pp. 1920–1923, jul 1996.

[5] F. Xia, H. Wang, D. Xiao, M. Dubey, and A. Ramasubramaniam, "Two-dimensional material nanophotonics," *Nature Photonics*, vol. 8, pp. 899–907, dec 2014.

[6] S. Wu, S. Buckley, J. R. Schaibley, L. Feng, J. Yan, D. G. Mandrus, F. Hatami, W. Yao, J. Vučković, A. Majumdar, and X. Xu, "Monolayer semiconductor nanocavity lasers with ultralow thresholds," *Nature*, vol. 520, pp. 69–72, apr 2015.

[7] L. D. Zhao, S. H. Lo, Y. Zhang, H. Sun, G. Tan, C. Uher, C. Wolverton, V. P. Dravid, and M. G. Kanatzidis, "Ultralow thermal conductivity and high thermoelectric figure of merit in SnSe crystals," *Nature*, vol. 508, pp. 373–377, apr 2014.

[8] J. S. Kang, H. Wu, M. Li, and Y. Hu, "Intrinsic Low Thermal Conductivity and Phonon Renormalization Due to Strong Anharmonicity of Single-Crystal Tin Selenide," *Nano Letters*, vol. 19, pp. 4941–4948, aug 2019.

[9] M. Amani, D. H. Lien, D. Kiriya, J. Xiao, A. Azcatl, J. Noh, S. R. Madhvapathy, R. Addou, K. C. Santosh, M. Dubey, K. Cho, R. M. Wallace, S. C. Lee, J. H. He, J. W. Ager, X. Zhang, E. Yablonovitch, and A. Javey, "Near-unity photoluminescence quantum yield in MoS2," *Science*, vol. 350, no. 6264, pp. 1065–1068, 2015.

[10] Y. Ye, Z. Ye, M. Gharghi, H. Zhu, M. Zhao, Y. Wang, X. Yin, and X. Zhang, "Exciton-dominant electroluminescence from a diode of monolayer MoS_2," *Applied Physics Letters*, vol. 104, may 2014.

[11] M. H. Beck, A. Jäckle, G. A. Worth, and H. D. Meyer, "The multiconfiguration time-dependent Hartree (MCTDH) method: A highly efficient algorithm for propagating wavepackets," *Physics Report*, vol. 324, pp. 1–105, jan 2000.

[12] P. Güttinger, "Das Verhalten von Atomen im magnetischen Drehfeld," *Zeitschrift für Physik*, vol. 73, pp. 169–184, mar 1932.

[13] W. Pauli, "Principles of Wave Mechanics," in *Handbuch der Physik*, ch. 24, p. 162, Berlin: Springer, 1933.

[14] H. Hellmann, *Einführung in die Quantenchemie*. Leipzig: Franz Deuticke, 1937.

[15] R. P. Feynman, "Forces in molecules," *Physical Review*, vol. 56, pp. 340–343, aug 1939.

[16] M. Born and R. Oppenheimer, "Zur Quantentheorie der Molekeln," *Annalen der Physik*, vol. 389, pp. 457–484, 1927.

[17] L. Wang, R. Long, and O. V. Prezhdo, "Time-domain ab initio modeling of photoinduced dynamics at nanoscale interfaces.," *Annual review of physical chemistry*, vol. 66, pp. 549–79, 2015.

[18] R. Crespo-Otero and M. Barbatti, "Recent Advances and Perspectives on Nonadiabatic Mixed Quantum-Classical Dynamics," 2018.

[19] T. R. Nelson, A. J. White, J. A. Bjorgaard, A. E. Sifain, Y. Zhang, B. Nebgen, S. Fernandez-Alberti, D. Mozyrsky, A. E. Roitberg, and S. Tretiak, "Non-adiabatic Excited-State Molecular Dynamics: Theory and Applications for Modeling Photophysics in Extended Molecular Materials," *Chemical Reviews*, vol. 120, pp. 2215–2287, feb 2020.

[20] B. F. E. Curchod and T. J. Martínez, "Ab Initio Nonadiabatic Quantum Molecular Dynamics," *Chemical Reviews*, vol. 118, no. 7, pp. 3305–3336, 2018.

[21] J. C. Tully, "Molecular dynamics with electronic transitions," *The Journal of Chemical Physics*, vol. 93, no. 2, p. 1061, 1990.

[22] A. V. Akimov and O. V. Prezhdo, "The PYXAID program for non-adiabatic molecular dynamics in condensed matter systems," *Journal of Chemical Theory and Computation*, vol. 9, pp. 4959–4972, nov 2013.

[23] A. V. Akimov and O. V. Prezhdo, "Advanced capabilities of the PYXAID program: Integration schemes, decoherence effects, multiexcitonic states, and field-matter interaction," *Journal of Chemical Theory and Computation*, vol. 10, no. 2, pp. 789–804, 2014.

[24] E. Runge and E. K. U. Gross, "Density-functional theory for time-dependent systems," *Physical Review Letters*, vol. 52, no. 12, pp. 997–1000, 1984.

[25] A. Görling and M. Levy, "Exact Kohn-Sham scheme based on perturbation theory," *Physical Review A*, vol. 50, pp. 196–204, jul 1994.

[26] S. Sharma, J. K. Dewhurst, and C. Ambrosch-Draxl, "All-electron exact exchange treatment of semiconductors: Effect of core-valence interaction on band-gap and d-band position," *Physical Review Letters*, vol. 95, p. 136402, sep 2005.

[27] S. Sharma, J. K. Dewhurst, A. Sanna, and E. K. Gross, "Bootstrap approximation for the exchange-correlation kernel of time-dependent density-functional theory," *Physical Review Letters*, vol. 107, p. 186401, oct 2011.

[28] A. D. Algarno and J. T. Lewis, "The exact calculation of long-range forces between atoms by perturbation theory," *Proceedings of the Royal Society of London. Series A. Mathematical and Physical Sciences*, vol. 233, no. 1192, pp. 70–74, 2006.

[29] S. Baroni, S. de Gironcoli, A. Dal Corso, and P. Giannozzi, "Phonons and related crystal properties from density-functional perturbation theory," *Reviews of Modern Physics*, vol. 73, pp. 515–562, jul 2001.

[30] M. E. Casida, "Time-dependent density functional response theory of molecular

systems: Theory, computational methods, and functionals," *Theoretical and Computational Chemistry*, vol. 4, no. C, pp. 391–439, 1996.

[31] B. Sundaram and P. W. Milonni, "High-order harmonic generation: Simplified model and relevance of single-atom theories to experiment," *Physical Review A*, vol. 41, no. 11, pp. 6571–6573, 1990.

[32] M. Lewenstein, P. Balcou, M. Y. Ivanov, A. L'Huillier, and P. B. Corkum, "Theory of high-harmonic generation by low-frequency laser fields," *Physical Review A*, vol. 49, pp. 2117–2132, mar 1994.

[33] S. Ghimire, A. D. Dichiara, E. Sistrunk, P. Agostini, L. F. Dimauro, and D. A. Reis, "Observation of high-order harmonic generation in a bulk crystal," *Nature Physics*, vol. 7, pp. 138–141, feb 2011.

[34] S. Ghimire, A. D. Dichiara, E. Sistrunk, G. Ndabashimiye, U. B. Szafruga, A. Mohammad, P. Agostini, L. F. Dimauro, and D. A. Reis, "Generation and propagation of high-order harmonics in crystals," *Physical Review A - Atomic, Molecular, and Optical Physics*, vol. 85, no. 4, p. 43836, 2012.

[35] G. Ndabashimiye, S. Ghimire, M. Wu, D. A. Browne, K. J. Schafer, M. B. Gaarde, and D. A. Reis, "Solid-state harmonics beyond the atomic limit," *Nature*, vol. 534, pp. 520–523, jun 2016.

[36] H. Liu, Y. Li, Y. S. You, S. Ghimire, T. F. Heinz, and D. A. Reis, "High-harmonic generation from an atomically thin semiconductor," *Nature Physics*, vol. 13, pp. 262–265, mar 2017.

[37] S. Ghimire and D. A. Reis, "High-harmonic generation from solids," *Nature Physics*, vol. 15, pp. 10–16, jan 2019.

[38] S. Sharma and C. Ambrosch-Draxl, "Second-harmonic optical response from first principles," *Physica Scripta T*, vol. 109, pp. 128–134, 2004.

[39] N. Tancogne-Dejean, O. D. Mücke, F. X. Kärtner, and A. Rubio, "Ellipticity dependence of high-harmonic generation in solids originating from coupled intraband and interband dynamics," *Nature Communications*, vol. 8, no. 1, 2017.

[40] N. Tancogne-Dejean, O. D. Mücke, F. X. Kärtner, and A. Rubio, "Impact of the Electronic Band Structure in High-Harmonic Generation Spectra of Solids," *Physical Review Letters*, vol. 118, no. 8, 2017.

[41] N. Tancogne-Dejean and A. Rubio, "Atomic-like high-harmonic generation from two-dimensional materials," *Science Advances*, vol. 4, p. 5207, feb 2018.

[42] J. C. Baggesen and L. B. Madsen, "On the dipole, velocity and acceleration forms in high-order harmonic generation from a single atom or molecule," *Journal of Physics B: Atomic, Molecular and Optical Physics*, vol. 44, p. 115601, jun 2011.

[43] L. H. Thomas, "The calculation of atomic fields," *Mathematical Proceedings of the Cambridge Philosophical Society*, vol. 23, no. 05, pp. 542–548, 1927.

[44] E. Fermi, "Un Metodo Statistico per la Determinazione di alcune Prioprietà dell'Atomo," *Rend. Accad. Naz. Lincei*, vol. 6, pp. 602–607, 1927.

[45] P. A. M. Dirac, "Note on exchange phenomena in the Thomas atom," *Mathematical Proceedings of the Cambridge Philosophical Society*, vol. 26, no. 03, pp. 376–385, 1930.

[46] P. Hohenberg and W. Kohn, "Inhomogeneous Electron Gas," *Phys. Rev.*, vol. 136, pp. B864—-B871, nov 1964.

[47] W. Kohn and L. J. Sham, "Self-Consistent Equations Including Exchange and

Correlation Effects," *Phys. Rev.*, vol. 140, pp. A1133–A1138, nov 1965.

[48] T. Koopmans, "Über die Zuordnung von Wellenfunktionen und Eigenwerten zu den Einzelnen Elektronen Eines Atoms," *Physica*, vol. 1, pp. 104–113, jan 1934.

[49] J. P. Perdew, K. Burke, and M. Ernzerhof, "Generalized gradient approximation made simple," *Physical Review Letters*, vol. 77, no. 18, pp. 3865–3868, 1996.

[50] N. W. Ashcroft and N. D. Mermin, *Solid state physics*. Tokyo; Philadelphia: Saunders College, 1976.

[51] P. Giannozzi, S. Baroni, N. Bonini, M. Calandra, R. Car, C. Cavazzoni, D. Ceresoli, G. L. Chiarotti, M. Cococcioni, I. Dabo, A. Dal Corso, S. De Gironcoli, S. Fabris, G. Fratesi, R. Gebauer, U. Gerstmann, C. Gougoussis, A. Kokalj, M. Lazzeri, L. Martin-Samos, N. Marzari, F. Mauri, R. Mazzarello, S. Paolini, A. Pasquarello, L. Paulatto, C. Sbraccia, S. Scandolo, G. Sclauzero, A. P. Seitsonen, A. Smogunov, P. Umari, and R. M. Wentzcovitch, "Quantum ESPRESSO: A modular and open-source software project for quantum simulations of materials," *Journal of Physics Condensed Matter*, vol. 21, p. 395502, sep 2009.

[52] P. Giannozzi, O. Andreussi, T. Brumme, O. Bunau, M. Buongiorno Nardelli, M. Calandra, R. Car, C. Cavazzoni, D. Ceresoli, M. Cococcioni, N. Colonna, I. Carnimeo, A. Dal Corso, S. De Gironcoli, P. Delugas, R. A. Distasio, A. Ferretti, A. Floris, G. Fratesi, G. Fugallo, R. Gebauer, U. Gerstmann, F. Giustino, T. Gorni, J. Jia, M. Kawamura, H. Y. Ko, A. Kokalj, E. Kücükbenli, M. Lazzeri, M. Marsili, N. Marzari, F. Mauri, N. L. Nguyen, H. V. Nguyen, A. Otero-De-La-Roza, L. Paulatto, S. Poncé, D. Rocca, R. Sabatini, B. Santra, M. Schlipf, A. P. Seitsonen, A. Smogunov, I. Timrov, T. Thonhauser, P. Umari, N. Vast, X. Wu, and S. Baroni, "Advanced capabilities for materials modelling with Quantum ESPRESSO," *Journal of Physics Condensed Matter*, vol. 29, p. 465901, nov 2017.

[53] G. Kresse and J. Hafner, "Ab initio molecular dynamics for liquid metals," *Physical Review B*, vol. 47, no. 1, pp. 558–561, 1993.

[54] G. Kresse and J. Furthmüller, "Efficient iterative schemes for ab initio total-energy calculations using a plane-wave basis set," *Physical Review B - Condensed Matter and Materials Physics*, vol. 54, no. 16, pp. 11169–11186, 1996.

[55] G. Kresse and J. Furthmüller, "Efficiency of ab-initio total energy calculations for metals and semiconductors using a plane-wave basis set," *Computational Materials Science*, vol. 6, pp. 15–50, jul 1996.

[56] J. M. Soler, E. Artacho, J. D. Gale, A. García, J. Junquera, P. Ordejón, and D. Sánchez-Portal, "The SIESTA method for ab initio order-N materials simulation," *Journal of Physics: Condensed Matter J. Phys.: Condens. Matter*, vol. 14, pp. 2745–2779, 2002.

[57] D. J. Singh and L. Nordström, *Planewaves, pseudopotentials and the LAPW method: Second edition*. 2006.

[58] W. Quester, "Pseudopotential."
https://commons.wikimedia.org/w/index.php?curid=10227075.

[59] A. Togo, L. Chaput, and I. Tanaka, "Distributions of phonon lifetimes in Brillouin zones," *Physical Review B - Condensed Matter and Materials Physics*, vol. 91, no. 9, p. 94306, 2015.

[60] A. Togo and I. Tanaka, "First principles phonon calculations in materials science," *Scripta Materialia*, vol. 108, pp. 1–5, nov 2015.

[61] P. Maldonado, K. Carva, M. Flammer, and P. M. Oppeneer, "Theory of out-of-equilibrium ultrafast relaxation dynamics in metals," *Physical Review B*, vol. 96, no. 17, p. 174439, 2017.

[62] P. B. Allen, "Theory of thermal relaxation of electrons in metals," *Physical Review Letters*, vol. 59, no. 13, pp. 1460–1463, 1987.

[63] R. Xu and T. C. Chiang, "Determination of phonon dispersion relations by X-ray thermal diffuse scattering," *Zeitschrift fur Kristallographie*, vol. 220, no. 12, pp. 1009–1016, 2005.

[64] P. Maldonado, T. Chase, A. H. Reid, X. Shen, R. K. Li, K. Carva, T. Payer, M. Horn Von Hoegen, K. Sokolowski-Tinten, X. J. Wang, P. M. Oppeneer, and H. A. Dürr, "Tracking the ultrafast nonequilibrium energy flow between electronic and lattice degrees of freedom in crystalline nickel," *Physical Review B*, vol. 101, no. 10, p. 100302, 2020.

[65] B. Radisavljevic, A. Radenovic, J. Brivio, V. Giacometti, and A. Kis, "Single-layer MoS2 transistors," *Nature Nanotechnology*, vol. 6, pp. 147–150, mar 2011.

[66] Q. H. Wang, K. Kalantar-Zadeh, A. Kis, J. N. Coleman, and M. S. Strano, "Electronics and optoelectronics of two-dimensional transition metal dichalcogenides," *Nature Nanotechnology*, vol. 7, pp. 699–712, nov 2012.

[67] D. Pariari and D. D. Sarma, "Nature and origin of unusual properties in chemically exfoliated 2D MoS2," *APL Materials*, vol. 8, p. 040909, apr 2020.

[68] B. Smith, M. Shakiba, and A. V. Akimov, "Nonadiabatic Dynamics in Si and CdSe Nanoclusters: Many-Body vs Single-Particle Treatment of Excited States," *Journal of Chemical Theory and Computation*, vol. 17, pp. 678–693, feb 2021.

[69] B. Smith, M. Shakiba, and A. V. Akimov, "Crystal Symmetry and Static Electron Correlation Greatly Accelerate Nonradiative Dynamics in Lead Halide Perovskites," *The Journal of Physical Chemistry Letters*, vol. 12, pp. 2444–2453, mar 2021.

[70] A. F. Izmaylov and G. E. Scuseria, "Why are time-dependent density functional theory excitations in solids equal to band structure energy gaps for semilocal functionals, and how does nonlocal Hartree-Fock-type exchange introduce excitonic effects?," *Journal of Chemical Physics*, vol. 129, p. 034101, jul 2008.

[71] G. Granucci, M. Persico, and A. Zoccante, "Including quantum decoherence in surface hopping," *Journal of Chemical Physics*, vol. 133, p. 134111, oct 2010.

[72] A. V. Akimov, "A Simple Phase Correction Makes a Big Difference in Nonadiabatic Molecular Dynamics," *Journal of Physical Chemistry Letters*, vol. 9, pp. 6096–6102, oct 2018.

[73] A. V. Akimov, "Libra: An open-Source methodology discovery library for quantum and classical dynamics simulations," *Journal of Computational Chemistry*, vol. 37, pp. 1626–1649, jun 2016.

[74] L. Li, R. Long, T. Bertolini, and O. V. Prezhdo, "Sulfur Adatom and Vacancy Accelerate Charge Recombination in MoS_2 but by Different Mechanisms: Time-Domain Ab Initio Analysis," *Nano Letters*, vol. 17, no. 12, pp. 7962–7967, 2017.

[75] L. Li, R. Long, and O. V. Prezhdo, "Why Chemical Vapor Deposition Grown MoS$_2$ Samples Outperform Physical Vapor Deposition Samples: Time-Domain ab Initio Analysis," *Nano Letters*, vol. 18, no. 6, pp. 4008–4014, 2018.

[76] K. F. Mak, C. Lee, J. Hone, J. Shan, and T. F. Heinz, "Atomically thin MoS$_2$: A new direct-gap semiconductor," *Physical Review Letters*, vol. 105, p. 136805, sep 2010.

[77] K. I. Bolotin, K. J. Sikes, Z. Jiang, M. Klima, G. Fudenberg, J. Hone, P. Kim, and H. L. Stormer, "Ultrahigh electron mobility in suspended graphene," *Solid State Communications*, vol. 146, pp. 351–355, jun 2008.

[78] A. A. Balandin, S. Ghosh, W. Bao, I. Calizo, D. Teweldebrhan, F. Miao, and C. N. Lau, "Superior thermal conductivity of single-layer graphene," *Nano Letters*, vol. 8, pp. 902–907, mar 2008.

[79] C. Lee, X. Wei, J. W. Kysar, and J. Hone, "Measurement of the elastic properties and intrinsic strength of monolayer graphene," *Science*, vol. 321, pp. 385–388, jul 2008.

[80] Y. Cao, V. Fatemi, S. Fang, K. Watanabe, T. Taniguchi, E. Kaxiras, and P. Jarillo-Herrero, "Unconventional superconductivity in magic-angle graphene superlattices," *Nature*, vol. 556, pp. 43–50, apr 2018.

[81] W. L. Wang, S. Meng, and E. Kaxiras, "Graphene NanoFlakes with large spin," *Nano Letters*, vol. 8, no. 1, pp. 244–245, 2008.

[82] A. M. Silva, M. S. Pires, V. N. Freire, E. L. Albuquerque, D. L. Azevedo, and E. W. Caetano, "Graphene nanoflakes: Thermal stability, infrared signatures, and potential applications in the field of spintronics and optical nanodevices," *Journal of Physical Chemistry C*, vol. 114, pp. 17472–17485, oct 2010.

[83] Y. W. Son, M. L. Cohen, and S. G. Louie, "Energy Gaps in Graphene Nanoribbons," *Physical Review Letters*, vol. 97, p. 216803, nov 2006.

[84] H. Lee, Y. W. Son, N. Park, S. Han, and J. Yu, "Magnetic ordering at the edges of graphitic fragments: Magnetic tail interactions between the edge-localized states," *Physical Review B - Condensed Matter and Materials Physics*, vol. 72, p. 174431, nov 2005.

[85] C. Mansilla Wettstein, F. P. Bonafé, M. B. Oviedo, and C. G. Sánchez, "Optical properties of graphene nanoflakes: Shape matters," *Journal of Chemical Physics*, vol. 144, p. 224305, jun 2016.

[86] D. Bansal, J. Hong, C. W. Li, A. F. May, W. Porter, M. Y. Hu, D. L. Abernathy, and O. Delaire, "Phonon anharmonicity and negative thermal expansion in SnSe," *Physical Review B*, vol. 94, p. 054307, aug 2016.

Acta Universitatis Upsaliensis

Digital Comprehensive Summaries of Uppsala Dissertations
from the Faculty of Science and Technology 2028

Editor: The Dean of the Faculty of Science and Technology

A doctoral dissertation from the Faculty of Science and
Technology, Uppsala University, is usually a summary of a
number of papers. A few copies of the complete dissertation
are kept at major Swedish research libraries, while the
summary alone is distributed internationally through
the series Digital Comprehensive Summaries of Uppsala
Dissertations from the Faculty of Science and Technology.
(Prior to January, 2005, the series was published under the
title "Comprehensive Summaries of Uppsala Dissertations
from the Faculty of Science and Technology".)

Ā
UU

ACTA
UNIVERSITATIS
UPSALIENSIS
UPPSALA
2021